

Thermodynamics, Kinetics, and Optical Properties of Rotaxanes: A First-Principles Molecular Dynamics Study

Gourhari Jana and Jose L. Mendoza-Cortes*



Cite This: *J. Phys. Chem. A* 2023, 127, 2671–2687



Read Online

ACCESS |



Metrics & More

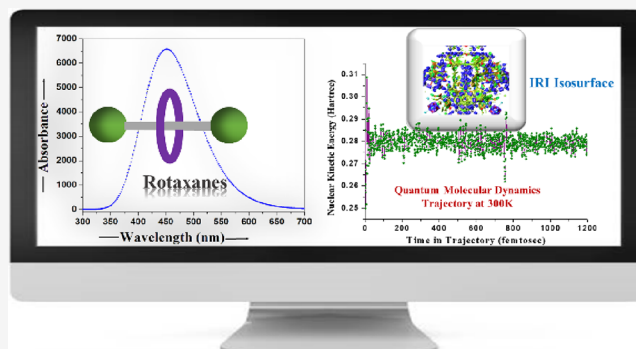


Article Recommendations



Supporting Information

ABSTRACT: Through molecular mechanics using the force field along with the quantum dynamical aspect of mechanically interlocked compounds, rotaxanes (defined as macromolecular rings that are threaded on a dumbbell-shaped axle molecule) are investigated with advanced quantum mechanical methods, including the atom-centered density matrix propagation simulation technique, at different temperatures like 300, 500, 700, 900, 2000, and 2500 K for 1.2 ps. *Ab initio* molecular dynamics simulation is carried out. In addition to, we investigate the noncovalent interaction present in the rotaxane compound 2R-D-2PF₆ with the help of reduced density gradient, average reduced density gradient, density overlap region indicator, and interaction region indicator as well as Hirshfeld surface analyses. Furthermore, the stability of 2R-D-2PF₆ at room temperature and higher temperatures is elucidated by analyzing the thermal fluctuation index through a dynamic process. In order to check the optical behavior of our selected rotaxane compound, an evaluation of the electronic dipole moment, static and frequency-dependent average polarizability, and first- and second-order hyperpolarizability is carried out. The rotaxane compound shows very promising linear and nonlinear optical responses, which indicates its utility as a very good optical material. The calculation of the time-dependent density-functional theory highlights the broad absorption band of rotaxane spanning the UV–visible domain. Therefore, we also unravel that this can tap into solar radiation or harnessing of solar energy.



1. INTRODUCTION

Molecules having mechanical bonds have always fascinated synthetic chemists and have been a highlight of extreme interest for them as they are exploited for the construction of a variety of new materials and molecular machines.^{1,2} Rotaxanes are a subclass of mechanically interlocked compounds next to molecular knots and catenanes.³ Rotaxanes are composed of two units: (i) “macrocyclic” molecules and (ii) threads or axle (“axle” molecule end-capped with bulky groups called stoppers or dumbbells, where the separation of both units is hindered by terminal bulky stoppers of the thread). In general, rotaxane compounds containing one thread and one macrocycle are the most common type of mechanically interlocked compounds, and higher-order rotaxane [*n*] compounds containing several threads and/or macrocycles are rarely employed. The amazing properties and potential use of rotaxanes in promising application fields^{4–10} make them highly attractive to the growing interest of the scientific community. For the most important invention of molecular machines, Sir J. Fraser Stoddart, Jean-Pierre Sauvage, and Bernard L. Feringa were awarded the Nobel Prize in Chemistry in 2016.^{11–13} For the synthesis of rotaxane compounds, the most commonly used strategies are clipping, capping, and slipping.¹⁴ Rotaxanes of higher complexity or order are prepared through the clipping mechanism.^{15–17} The imine bond formation is reversible, which

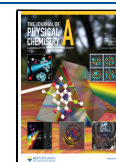
is again one of the most popular clipping reactions. When this bond formation reaction is combined with template-directed noncovalent interactions (NCIs) (Coulombic and dispersion interactions), it gives rise to a high yield of synthetic products.¹⁸

We performed rotaxane formation through imine bond formation. There are two types of dumbbells (abbreviated as D and Dp) at both the stopper ends of the “axle” molecule, which contains two recognition sites $-\text{C}_6\text{H}_4(\text{OCH}_3)_2$ and $-\text{NH}_2^+$ (they are also called “stoppers” as they retard the macrocyclic molecules to come out from the “axle” thread) (see Scheme 1).¹⁹ However, the separation of these dumbbells makes them distinct from each other and plays an important role in kinetics and thermodynamics. The separate threads excluding D and Dp dumbbells are given by $-\text{[CH}_2\text{CH}_2\text{NH}_2^+\text{CH}_2\text{]}_n^-$ and $-\text{[C}_6\text{H}_4\text{CH}_2\text{NH}_2^+\text{CH}_2\text{]}_n^-$, respectively, for our present study (see Scheme 1). The template-directed synthesis is observed in one case, but it is not observed in another case. These two cases

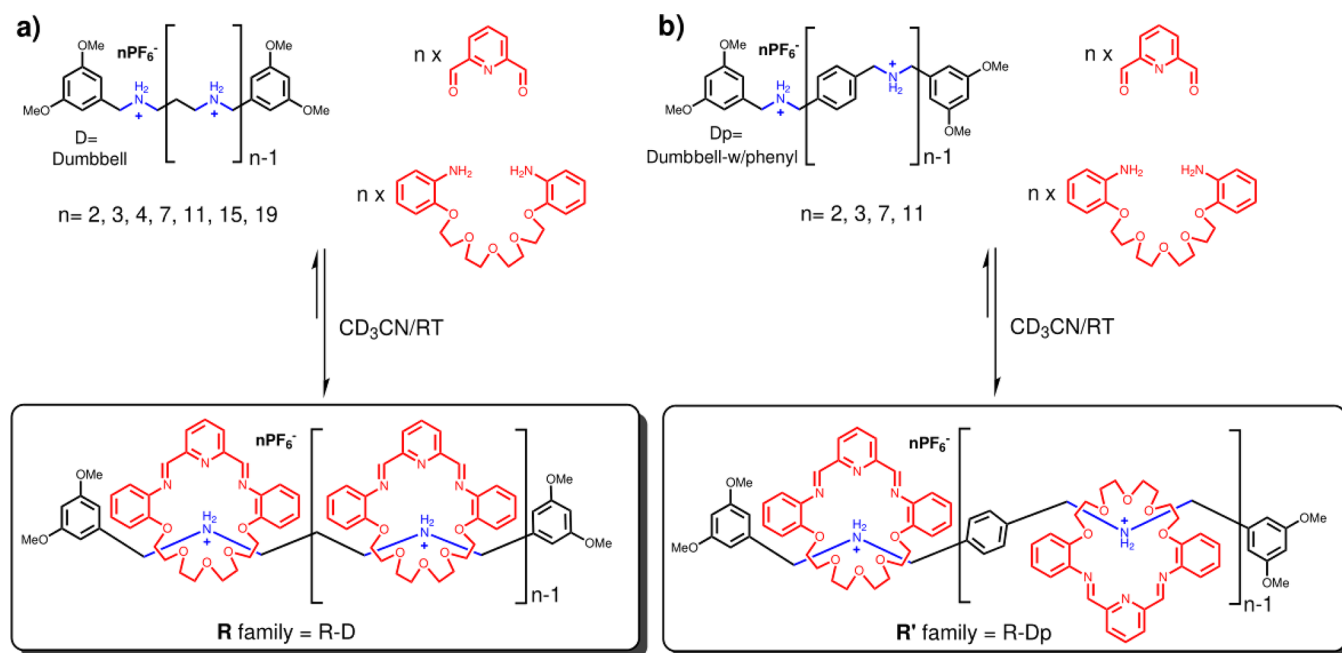
Received: November 4, 2022

Revised: February 23, 2023

Published: March 15, 2023



Scheme 1. Reaction for the Template-Directed Formation of Rotaxanes for the (a) R Family and (b) R' Family



are differentiated by an experimental procedure, although this distinction based on quantitative energy calculation is not transparent. In our present work, we observed that the maintenance of reaction efficiency in the R series can be ascribed to positive cooperativity; that is, when one ring is formed, it aids and abets the formation of subsequent rings presumably because of stabilizing extended $\pi\cdots\pi$ stacking interactions between the arene units. Experiments have been performed wherein the dumbbell is starved of the macrocyclic components, and up to five times more of the fully saturated rotaxane is formed than is predicted based on a purely statistical outcome, providing a clear indication that positive cooperativity is operative. Furthermore, we investigated the role of dispersion forces like van der Waals, hydrogen bonding, and $\pi\cdots\pi$ interactions including Coulombic interactions (counter anion) in the formation of these rotaxanes. The experimental observation is explained by our theoretical findings.

On the other hand, we are now focused on the dynamical behavior of the unbound wheel component and counter ions in our selected rotaxane compound through molecular mechanics Dreiding and the Optimized Potentials for Liquid Simulations (OPLS) force field method along with the *ab initio* molecular dynamics simulation technique (named atom-centered Density Matrix Propagation (ADMP) method) developed by Schlegel et al.^{20,21} ADMP is an extended Lagrangian procedure in which density matrix propagation in an atom-centered Gaussian basis function is used. The distinct advantage of the use of Gaussian orbitals is its leading toward sparse matrix representations for the density matrix and Hamiltonian in the large system limit.

Besides the great advantages of the ADMP method,^{22–24} it is reported that the ADMP trajectory is very much similar to the Born–Oppenheimer trajectory if we exclude the fictitious electronic mass effect on the adiabaticity and energy conservation.^{20,25} The former method is faster by three to four times than the latter if the step sizes of both methods remain the same. It also works with large time steps and offers good computational efficiency. In the present study, we used ADMP simulation because of its computational advantages (the

gradient-based integration scheme is cheaper than the Hessian-based predictor–corrector integration scheme for larger systems).

Again, the identification of the interaction between the unbound “macroscopic” component, “axle” molecule, and counter ions of the rotaxane compound is entangled by NCIs introduced by Johnson et al.,²⁶ based on the electron density especially $\text{sign}(\lambda_2)\rho$ in real space and its first derivative ($s = 1/(2(3\pi^2)^{1/3})|\nabla\rho|/\rho^{4/3}$). This pair of important functions is called reduced density gradient (RDG).

In order to distinguish the types of weak interactions present in the rotaxane compound, i.e., van der Waals (vdW), $\pi\cdots\pi$ stacking, hydrogen bonding (H-bonding), and steric repulsion, we considered the second derivative of the density. It is an important aspect that in order to analyze weak interactions throughout the molecular dynamics trajectory or fluctuation environment, the extended NCI method called averaged NCI (aNCI)²⁷ over multiple frames (1200 frames are used in the present study to generate an aNCI graph) is used. We also employed new indicators such as thermal fluctuation index (TFI), density overlap regions indicator (DORI),²⁸ and interaction region indicator (IRI)²⁹ to describe both covalent and NCIs in the rotaxane.

Furthermore, the rotaxane compound is found to show interesting linear and nonlinear optical (NLO) properties as understood by the evaluation of the static and dynamic average polarizability (α_{av}), first-order hyperpolarizability (β), and second-order hyperpolarizability (γ). When certain materials are subjected to interact with an optical field (light) of a given frequency, the electronic cloud of these materials will oscillate in the knock of the beam. In a linear absorption process, this oscillation will be referenced as harmonic in mechanics with the incident light frequency and the absorbed light would be remitted as a secondary radiation of the same frequency. However, in a nonlinear process, the oscillating electronic motion will ultimately become anharmonic and reemit light having a different frequency and amplitude from the incident beam. These features have many important practical applica-

tions in the electrical and optical industries. As rotaxanes belong to a very distinct class composed of mobile parts, the component molecules are mechanically bound and held together in an attractive architecture, which can have NLO activity.

Therefore, we discussed to explore the optoelectronic behavior of our selected rotaxane compounds and their possible potential application in the fields of optoelectronics (optical data storage, integrated optics, optical sensing, optical switching, optical signal processing, optical computing, optical modulators, photonics optical signal processing, optical limiting, optical communication technology,^{30–32} quantum computing,³³ and so on), nanophotonics, etc.

2. METHODOLOGY AND COMPUTATIONAL DETAILS

2.1. Molecular Mechanics. To generate plausible geometries for higher-order rotaxanes, MM including the force field (FF) validation is necessary to use as a key step. We performed analyses using the Dreiding³⁴ and OPLS³⁵ force fields (inbuilt in this FF) in our present study and compared them with the QM calculations. The charges for Dreiding are obtained from Qeq.³⁶ We employed the conjugated gradient minimization method. The minimization step stops when the convergence criterion of 0.05 kcal/mol is met or it runs up to at least 5000 steps.

2.2. Quantum Mechanics. We started with the experimentally synthesized structures and optimized all the geometries using the M06-L functional^{37,38} in conjunction with the 6-31G** basis set^{39,40} and the LAV3P** basis⁴¹ with the effective core potential (ECP) used for I as implemented in Jaguar.⁴² Optimization of all the geometries is carried out using the analytical Hessian method. There is no imaginary frequency, confirming that the geometries exist in local minima. To compute the zero-point-corrected energy at 0 K, vibrational frequencies are used from the analytical Hessian method. Solvent corrections are incorporated taking acetonitrile as solvent (in the Jaguar code, $R_0 = 2.18$ and $E = 37.5$ are implemented in the PBF module⁴³), and the single-point self-consistent Poisson–Boltzmann continuum solvation model is considered here. This methodology used in our study is corroborated by experimental observations.⁴⁴

Geometry optimization and the generation of the electronic wavefunction are carried out using Gaussian 16 C.01.⁴⁵ The highly parameterized meta-GGA approximation-based Minnesota functional M06-L^{37,38} is used for geometry optimization, molecular dynamics study, and electronic wavefunction generation in combination with the 6-31G(d) basis set.⁴⁶

ADMP trajectories are investigated at various temperatures like 300, 500, 700, 900, 2000, and 2500 K (called target or microscopic temperatures) up to 1.2 ps time duration integrated with a step size of 1 fs per simulation step. We used velocity scaling and the temperature-dependent thermostat approach employing ADMP implemented in the Gaussian 16 Program Package. A few internal options (IOps) are set for the ADMP simulation technique such as IOp(1/80 = 1,000,000), which is used to turn on velocity scaling thermostat, IOp(1/81 = 1) is used for frequency to check the thermostat (every “1” step), IOp(1/82 = 300) is used to declare the target temperature for NKE (in kelvin), and IOp(1/89 = 1) is used to allow deviation from the target temperature (in kelvin). In general, ADMP simply reevaluates the temperature every N time steps (where N is given in “IOp(1/81 = N)”). If the temperature differs from the target temperature T (where T is given by “IOp(1/82 = T)”) by more than D degrees (where D is given by “IOp(1/89 = D)”), we requested for our simulation study, $D = 1$, i.e., $T = 300 \text{ K} \pm 1 \text{ K}$,

and so on), and then the velocities are scaled (all of them are multiplied by a number either to increase them or decrease them) so the target temperature at the next time step becomes equal to T .

The aNCI analysis is performed with the Multiwfn code.⁴⁷ The 25 Å radius cutoff is chosen to compute the indices. Numbers of 80, 80, and 80 cube grid points are considered along each of the x , y , and z directions for average reduced density gradient (aRDG) and average $\text{sign}(\lambda_2)\rho$. VMD 1.9.3⁴⁸ is used for making 3D visualization plots of RDG, aRDG, TFI, DORI, and IRI. The color scale for the aNCI analysis and fluctuation index ranges $[-2, 2]$ and $[0, 1.5]$, respectively, and the threshold for RDG/aRDG is chosen to be 0.25.

In order to ascertain the linear and nonlinear responsive properties, we analyzed α_{av} , β , and γ . In the linear response case and in the presence of a weak electric field, the displacement of charges in a system from the equilibrium positions, i.e., polarization (P), is directly proportional to the applied electric field, E .

$$P = \alpha E \quad (1)$$

where α is called linear polarizability (tensor of rank 2). According to Kleinman's symmetry relations, the static α_{av} is calculated by using the following equation:⁴⁹

$$\alpha_{\text{av}} = 1/3(\alpha_{xx} + \alpha_{yy} + \alpha_{zz}) \quad (2)$$

where $\alpha_{xx/yy/zz}$ are the diagonal polarizability tensor components.

On the other hand, in the case of the nonlinear optical material, the oscillation of charges in a system is the nonlinear function of the electric field. In a very high intensity electric field, i.e., on exposure to laser light, the displacement of charge from its equilibrium position results in the behavior of polarizability of all materials beyond a linear regime.^{50,51} Nonlinear polarization can be represented as

$$P = P_0 + \chi^{(1)}E + \chi^{(2)}E^2 + \chi^{(3)}E^3 + \dots \quad (3)$$

The computed first hyperpolarizability, β , contains 27 tensor components (tensor of rank 3). The Kleinman symmetry allows reducing these 27 components of second harmonic generation $\beta(2\omega; \omega, \omega)$ into 10 in the general case of a molecule having no symmetry because of an independent interchange of cartesian coordinates, $\beta_{ijk} = \beta_{ikj} = \beta_{xxx} \beta_{xxx} \beta_{xyy} \beta_{xyy} \beta_{yyy} \beta_{xxx} \beta_{xyy} \beta_{yyy} \beta_{xxx} \beta_{xyy} \beta_{yyy}$ and β_{zzz} are 10 irreducible tensor components. We computed the orientationally averaged hyperpolarizabilities β ,^{49,52–55} taking the tensor product of these 10 irreducible elements. The below given equations help to calculate static and frequency-dependent first hyperpolarizability,

$$\beta(0; 0, 0) = \sqrt{(\beta_x^2 + \beta_y^2 + \beta_z^2)}(0; 0, 0) \quad (4)$$

$$\beta(-\omega; \omega, 0) = \sqrt{(\beta_x^2 + \beta_y^2 + \beta_z^2)}(-\omega; \omega, 0) \quad (5)$$

$$\beta(-2\omega; \omega, \omega) = \sqrt{(\beta_x^2 + \beta_y^2 + \beta_z^2)}(-2\omega; \omega, \omega) \quad (6)$$

$$\text{where } \beta_i = \sum_k \beta_{ikk}/3; i = x, y, z \quad (7)$$

According to electric dipole approximation, out of 10 tensor components, β_{xyz} is the only chiral component of the medium whereas the other nine components are achiral. The value of the chiral component β_{xyz} is zero due to the property of symmetric

tensor product basis set elements. However, it contributes majorly as a nonzero element to the macroscopic second-order polarizability tensor. Thus, the β_{xyz} component pertains significance while designing the molecule with a high β value in macroscopic perception. More symmetric molecules will have small chiral component β_{xyz} and they are so called less chiral molecules.

The frequency-dependent α_{av} is calculated using the following equation:

$$\alpha_{av}(-\omega; \omega) = 1/3 \sum_i \alpha_{ii}(-\omega; \omega) (i = x, y, \text{ and } z) \quad (8)$$

The anisotropy of the polarizability $\Delta\alpha$ is calculated using the expression

$$\Delta\alpha = \sqrt{[(\alpha_{xx} - \alpha_{yy})^2 + (\alpha_{yy} - \alpha_{zz})^2 + (\alpha_{zz} - \alpha_{xx})^2 + 6(\alpha_{xy}^2 + \alpha_{yz}^2 + \alpha_{xz}^2)]} \quad (9)$$

The second-order hyperpolarizability (γ) is the third-order response of the dipole moment, and the static and frequency-dependent ones are calculated using the following equations:

$$\gamma = 1/5[\gamma_{xxxx} + \gamma_{yyyy} + \gamma_{zzzz} + 2(\gamma_{xxyy} + \gamma_{xxzz} + \gamma_{yyzz})] \quad (10)$$

$$\gamma(-\omega; \omega, 0, 0) = 1/5 \sum_{i,j} \gamma_{ijij}(-\omega; \omega, 0, 0) \quad (11)$$

for the electro-optical Pockels effect and

$$\gamma(-2\omega; \omega, \omega, 0) = 1/5 \sum_{i,j} \gamma_{ijij}(-2\omega; \omega, \omega, 0) \quad (12)$$

for electric-field-induced second harmonic generation, respectively.

α_{ij} represents the linear polarizability, and γ_{ijkl} represents second-order hyperpolarizability tensor components.

All the frequency-dependent polarizabilities and microscopic first hyperpolarizability values are computed at the laser frequency of 1064 nm (0.0428 au) corresponding to the Nd:YAG frequency, as the Nd:YAG laser frequency is the best choice because of its wide applications in many hyper-Rayleigh scattering experiments and such choices overcome the resonance enhancement effects. In order to provide some rationale behind the observed NLO properties, we performed TDDFT calculations at the M06-L/6-31G(d) level where only singlet-to-singlet (spin-allowed) transitions are considered and 10 vertically excited electronic states are considered.

3. RESULTS AND DISCUSSION

3.1. Experimental Coordinates vs Molecular Mechanics vs Quantum Mechanics. We compared the coordinates from X-ray diffraction (XRD) and the minimum energy geometries extracted from quantum mechanics (QM) and molecular mechanics (MM) to verify the validity of our methodology for rotaxane compounds. The configurations are presented in Figures S1 and S2. It is found that the MM method provides good agreement with the experiment (the root mean square distance (RMSD) is around 0.350), while the QM provides relatively larger errors indicated by the RMSD value of 0.638, although we expected that QM will provide the best evaluation of the $\pi\cdots\pi$ interaction (see Table 1). The Dreiding FF comes next to QM. The estimations from the OPLS-FF are worst among all methodologies (see Figure S2). To ascertain the

Table 1. Root Mean Square Distance (RMSD) for the Comparison between Experimental Structures for 2R-2PF₆ and the QM and MM Methods^a

method	RMSD		RMSD
	Bz(D)-Bz(R1)	Bz(R1)-Bz(R2)	all atoms
experimental XRD	0	0	0
Dreiding2.21/Qeq	0.153	0.109	0.375
Dreiding3/Qeq	0.186	0.608	0.311
OPLS2005	0.235	0.446	0.320
MO6-L/6-31G**	0.152	0.106	0.638

^aColumns 2 and 3 show the estimation of the $R(\pi\cdots\pi)$ interaction for benzene (Bz) in the stopper of the dumbbell (D), first rotaxane (R1), and second rotaxane (R2).

formation of these structures, we assumed that the $\pi\cdots\pi$ stacking and other dispersion interactions have the key role and QM is more preferred than other methodologies.

Moreover, if we compare all the methodologies based on binding energy, the QM method provides us with a very consistent result. The binding energies for the first and second “macrocylic” rings in the gas phase are −26.1 and −60.6 kcal/mol, respectively, while OPLS-FF provides a strange result, i.e., the binding energies for the first and second “macrocylic” rings are −500 kcal/mol (quite high value) and +149 kcal/mol (indicating that the interaction is repulsive in nature) (see Table 2 and Figure S3). The MM method employing Dreiding FF is

Table 2. Comparison of Binding Energies for the Formation of 1R-2PF₆ and 2R-2PF₆^a

method	[1R]2PF ₆	[2R]2PF ₆
	gas phase	gas phase
Dreiding2.21/Qeq	35.7	52.5
Dreiding3/Qeq	32.7	22.8
OPLS2005	−500	149
MO6-L/6-31G**	−26.1	−60.6

^aAll the units are in kcal/mol.

unable to provide binding energies. Thus, QM is predicted to be the only method to represent appropriate results for expressing physically meaningful energetics of our studied rotaxane compounds.

Again, the times to reach equilibrium and reaction kinetics of the rotaxane compounds (both R and R' families) are determined by monitoring the clipping reaction by ¹H NMR spectroscopy until no changes are observed in the spectra. The related data are provided in Tables 3 and 4, respectively.

3.2. Origin of the Positive Cooperativity. The most important fact of this class of compounds is losing positive cooperativity due to the use of different dumbbells such as D and Dp (containing an extra phenyl group with D). We tried to find out the reason behind the loss of positive cooperativity by introducing different dumbbells. We predicted the geometries and calculated the thermochemical parameters like enthalpy and free energy changes for the rotaxane R family up to two “macrocylic” rings (shown in Figure S2). The experimental crystal structures for the R' family (rotaxanes with Dp) are unavailable, which is determined by our QM methodology with considerable accuracy. Because of the presence of an extra phenyl group in the R' family, the “macrocylic” rings (threaded over the “axle” molecule) get more separated and the interaction strength between these rings decreases. The forces involved in

Table 3. Reaction Kinetics on the Formation of the R Family, which Is the Combination of nR + D

compound no.	[n] rotaxane	rings	time to reach equilibrium ^a	isolated yield (%)	no. of imine bonds	yield per imine bond (%)
2R ²⁺	3	2	<5 min	93	4	98.2
3R ³⁺	4	3	<5 min	90	6	98.3
4R ⁴⁺	5	4	<5 min	88	8	98.4
7R ⁷⁺	8	7	6 h	94	14	99.6
11R ¹¹⁺	12	11	10 h	98	22	99.9
15R ¹⁵⁺	16	15	12 h	93	30	99.8
19R ¹⁹⁺	20	19	14 h	90	38	99.7

^aEquilibrium times are determined by monitoring the clipping reaction by ¹H NMR spectroscopy until no changes in the spectra are observed.

Table 4. Reaction Kinetics on the Formation of the R' Family, which Is the Combination of nR + Dp

compound no.	[n] rotaxane	rings	time to reach equilibrium ^a	isolated yield (%)	no. of imine bonds	yield per imine bond (%)
2R' ²⁺	3	2	<5 min	86	4	96.3
3R' ³⁺	4	3	<5 min	72	6	94.7
7R' ⁷⁺	8	7	20 min	78	8	98.2
11R' ¹¹⁺	12	11	30 min	85	14	99.3

^aEquilibrium times are determined by monitoring the clipping reaction by ¹H NMR spectroscopy until no changes in the spectra are observed.

these compounds are not quantified; even we do not have the idea about the changes in free energy and enthalpies for the interaction of the “macrocylic” rings with the 2-(C₆H₄CH₂)-NH₂⁺(CH₂)- or -(CH₂)NH₂⁺(CH₂)- site. It is also a very important part to quantify the hydrogen bonding interactions (N-H...O and N-H...N) involved in the systems. For this purpose, we calculated the interaction strength between the “stoppers” for both R and R' compounds along with the interaction strength between the -NH₂⁺- site of the “axle” molecule and the “macrocylic” rings threaded over it. It is found that the interaction between the “macrocylic” rings with the “stopper” is almost negligible, which is reflected in the free energy change (ΔG_{gas}) in the gas phase at -1.7 kcal/mol, while in acetonitrile, $\Delta G_{\text{CH}_3\text{CN}}$ is -3.2 kcal/mol. The interaction is almost similar for the R and R' families of compounds. Also, the interaction between the “macrocylic” rings with the -NH₂⁺- recognition site of -(C₆H₄CH₂)NH₂⁺(CH₂)- or -(CH₂)-NH₂⁺(CH₂)- is very close at ΔG_{gas} -25.4 and -26.7 kcal/mol, respectively. The ΔG_{solv} values in the solvent phase are quite different because of the inherent difference in the size of the -NH₂⁺- sites, one with a bigger moiety and another with a smaller one. For the bigger one, i.e., for -CH₂(Ph)NH₂⁺CH₂-, the value of $\Delta G_{\text{CH}_3\text{CN}}$ is -26.4 kcal/mol, while for the smaller one, -CH₂NH₂⁺CH₂-, the value of $\Delta G_{\text{CH}_3\text{CN}}$ is -22.3 kcal/mol (see Table 5). In the solvent phase, due to the presence of an extra -Ph group (i.e., -CH₂(Ph)NH₂⁺CH₂-) in between the macrocylic rings in the case of rotaxane compounds of the R' family, the solvent molecule gets enough space to penetrate and to interact with the -NH₂⁺- sites, while due to the close proximity of the -NH₂⁺- sites in the case of rotaxane compounds of the R family, the separation of bulky macro-molecules does not permit to penetrate the solvent molecules in

Table 5. ΔG_{gas} and ΔG_{solv} with Respect to Isolated Rotaxane Rings and Dumbbells

compounds	ΔH_{gas} (kcal/mol)	ΔG_{gas} (kcal/mol)	ΔG_{solv} (kcal/mol)
1R-(stopper site)	-16.3	-1.7	-3.2
R family			
1R-1R(4.0 Å) ^a	-26.6	-8.6	-8.8
1R-(NH ₂ site) ^b	-45.9	-26.7	-22.3
1R-D-2PF ₆	-41.2	-26.1	-33.1
2R-D-2PF ₆	-85.7	-60.6	-51.4
R' family			
1R-1R(5.0 Å) ^c	1.9	4.7	3.2
1R-(NH ₂ ' site) ^d	-43.3	-25.4	-26.4
1R-D-2PF ₆	-75.7	-60.6	-48.2
2R-D-2PF ₆	-45.7	-20.5	-25.1

^aThis is the rotaxane-rotaxane interaction distance for the 2R-D-2PF₆ system. ^bTo estimate the strength of this site, we used compound (CH₃)NH₂⁺(CH₃). ^cThis is the rotaxane-rotaxane interaction distance for the 2R-Dp-2PF₆ system. ^dTo estimate the strength of this site, we used compound (CH₃)NH₂⁺(C₆H₅CH₂).

between them, which inhibits the favorable interaction between -NH₂⁺- sites and solvent molecules. The result is that the charged -NH₂⁺- sites get more stabilized in the presence of acetonitrile solvent in the case of the R' family rather than in the case of the R family. However, in the case of the gas phase, there is no concern of solvent penetration and stabilization so the ΔG values in the gas phase are close despite the inherent differences in size of the -NH₂⁺- sites. The consequences are reflected in the solvent phase and the major distinction governed in the ΔG values in the presence of dipolar CH₃CN solvent molecules, i.e., the value of $\Delta G_{\text{CH}_3\text{CN}}$ for -CH₂(Ph)NH₂⁺CH₂- is bigger at -26.4 kcal/mol while the value of $\Delta G_{\text{CH}_3\text{CN}}$ for -CH₂NH₂⁺CH₂- is -22.3 kcal/mol.

Furthermore, we segregated the total interaction into three individual parts of interactions to locate the origin of the positive cooperativity. The interactions come from (i) two “macrocylic” rings, (ii) two “stoppers” (bulky groups at the end of the “axle” molecule), and (iii) two -NH₂⁺- recognition sites of the “axle” molecule for the R family. Our results in the gas phase indicate that the first “macrocylic” ring in 1R-D-2PF₆ only interacts with the -NH₂⁺- recognition site. The interaction strength between the “macrocylic” ring and the interacting -NH₂⁺- site in 1R-D-2PF₆ is almost the same as that of the interaction strength with the isolated -NH₂⁺- site, which is reflected in ΔG_{gas} : -26.7 kcal (for the former) and -26.1 kcal (for the latter). It is also noted that when the first “macrocylic” ring is threaded over the “axle” molecule, the interaction strength between the “macrocylic” ring and the “stoppers” is very low. This is observed from the optimized geometry of the rotaxane compounds (see Figure S2b), where the computed optimal distance between the pyridine ring of the “macrocylic” molecule and the dimethoxy benzene group of “stoppers” is 3.4 °Å. The solvation free energy (ΔG_{solv}) is 10 kcal/mol higher in solvent medium for the -NH₂⁺- recognition site than for the isolated -NH₂⁺- site. This is because of the size factor; 1R-D-2PF₆ (full system) has more surface area than the discrete unit, 1R-NH⁺(CH₃)₂. Thus, the solvation is more favorable in the case of the full system relative to considering the individual parts. However, the interaction between the “macrocylic” ring and the “stoppers” is recovered by the incorporation of a second “macrocylic” ring to the system, producing 2R-D-2PF₆. Therefore, it is inferred that the energetics of the full rotaxane

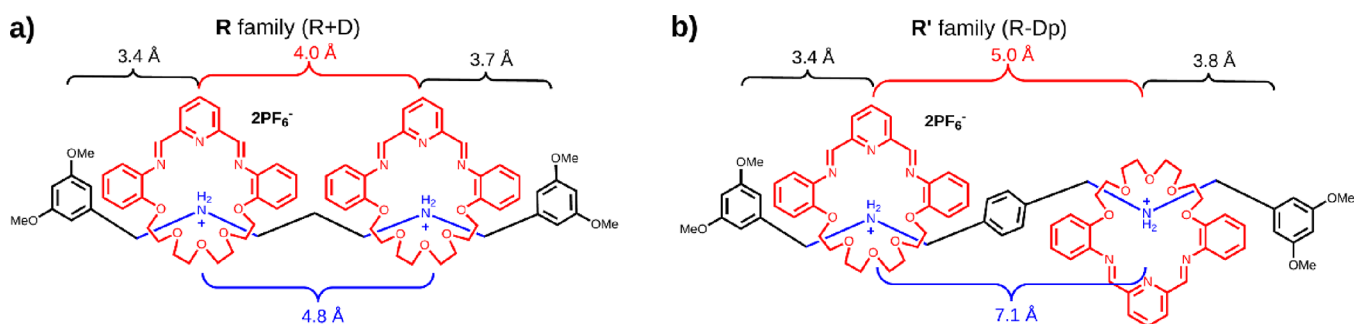


Figure 1. Distances for the optimized structure for (a) 2R-D-2PF₆ (R family) and (b) 2R-Dp-2PF₆ (R' family). In the R family, we observe a macrocyclic ring–macrocyclic ring interaction, while in the R' family, the distance between macrocyclic rings is too large for them to interact. The distance between the “stopper” and the “macrocyclic” ring is marked in black. The distance between the first and second macrocyclic rings is marked in red. The distance between the first and second –NH₂⁺– sites is marked in blue. The optimal “macrocyclic” ring–“macrocyclic” ring interaction distance is 3.6 °Å.

system with two “macrocyclic” rings, i.e., 2R-D-2PF₆ compound, is controlled by the interactions between two “macrocyclic” rings, two “macrocyclic” rings with “stoppers”, and two “macrocyclic” rings with the –NH₂⁺– sites. Therefore, the total interaction in the gas phase is the sum of all the individual interactions, i.e., $\Delta G_{\text{gas}}(\text{total}) = -8.6 \text{ kcal/mol}$ (“macrocyclic” ring – “macrocyclic” ring) + $-1.7 \times 2 \text{ kcal/mol}$ (two “macrocyclic” ring with two “stoppers”) + $-26.7 \times 2 \text{ kcal/mol}$ (two “macrocyclic” ring with two interacting –NH₂⁺– sites) = -65.4 kcal/mol [the free energy change from QM calculations for 2R-D-2PF₆ is -25.4 (first “macrocyclic” ring) – 60.6 (second “macrocyclic” ring) = -86.0 kcal/mol]. If the solvation effect is taken into consideration, we can partition it as $\Delta G_{\text{solv}}(\text{total}) = -8.8 \text{ kcal/mol}$ (“macrocyclic” ring – “macrocyclic” ring) + $-3.2 \times 2 \text{ kcal/mol}$ (two “macrocyclic” ring with two “stoppers”) + $-22.3 \times 2 \text{ kcal/mol}$ (two “macrocyclic” rings with two interacting –NH₂⁺– sites) = -59.8 kcal/mol [the free energy change from QM calculations for the 2R-D-2PF₆ compound in solvent is -51.4 (first “macrocyclic” ring) – 33.1 (second “macrocyclic” ring) = -84.5 kcal/mol]. ΔH_{gas} , ΔG_{gas} , and ΔG_{solv} are provided in Table 5. It is noted that the total free energy change for the rotaxane compound 2R-D-2PF₆ is higher than the sum of the individual contributions coming from segregated components for the positive cooperativity present in the system. Thus, this is a distinct case study where the interaction of free energy is higher when all the components exist together than when the individual components remain separately.

On the other hand, the first “macrocyclic” ring interacts not only with the dimethoxy benzene group that resides at the “stopper” end but also with the phenyl ring of the dumbbell Dp (see Figure S4b,e,h). We compared distances for the R and R' families (see Figure 1). In the optimized geometry of the 2R-Dp-2PF₆ compound (R family), we observe that the distance between “macrocyclic” ring and “macrocyclic” ring is 4.0 Å while in the case of the R' family, the distance is quite larger at 5.0 Å. The distance between the pyridine ring of the “macrocyclic” ring and the dimethoxy benzene ring at one “stopper” end is 3.4 Å, and on the other “stopper” end, it is 3.7 Å in the case of the R family, while in the case of the R' family, the distances are 3.4 and 3.8 Å, respectively. The distances between –NH₂⁺– sites are 4.8 and 7.1 Å for the R and R' families, respectively. The separation between different individual parts of the rotaxane compounds with dumbbell D and Dp reflects the change in energetics of the systems. In Figure S4, the computed ΔG_{gas} for the 1R-Dp-2PF₆ compound is -60.6 kcal/mol and ΔG_{solv} is -48.2 kcal/mol . The

interaction energies between 1 “macrocycle” and the –NH₂⁺– site are $\Delta G_{\text{gas}} = -25.4 \text{ kcal/mol}$ and $\Delta G_{\text{solv}} = -26.4 \text{ kcal/mol}$, and those between 1 “macrocycle” and the “stopper” are $\Delta G_{\text{gas}} = -1.7 \text{ kcal/mol}$ and $\Delta G_{\text{solv}} = -3.2 \text{ kcal/mol}$. The total interaction energies are $\Delta G_{\text{gas}} = -27.1 \text{ kcal/mol}$ and $\Delta G_{\text{solv}} = -29.6 \text{ kcal/mol}$, obtained by summing up these two individual interaction energies in both gas and solvent phases, which cannot be described by the total free energy changes for the full system of rotaxane compounds. The difference between the free energy changes ($\Delta G_{\text{gas}} = -33.5 \text{ kcal/mol}$ and $\Delta G_{\text{solv}} = -18.6 \text{ kcal/mol}$) obtained from the partition scheme and from the 1R-Dp-2PF₆ compound is assigned by the extra interaction coming from the “macrocyclic” ring and the phenyl group present next to the –NH₂⁺– site of the dumbbell Dp. When we add the second “macrocyclic” ring to both rotaxanes of the R and R' families, the main difference becomes obvious. The computed interaction free energy change in the gas phase is $\Delta G_{\text{gas}} = -20.5 \text{ kcal/mol}$ for the “macrocyclic” ring in the 2R-Dp-2PF₆ compound, which is close in interaction strength, i.e., $\Delta G_{\text{gas}} = -25.4 \text{ kcal/mol}$ for the interaction between the “macrocyclic” ring and the –NH₂⁺– site. In the solvent phase, the interaction free energy values are also compared and the values are almost the same. For the second “macrocyclic” ring in the 2R-Dp-2PF₆ compound, the interaction free energy changes (ΔG_{solv}) in the solvent phase are -25.1 and -26.4 kcal/mol for the interaction between the “macrocyclic” ring and the –NH₂⁺– site, respectively. This indicates a good validation of the results in the gas phase as well as in the solvent phase. It is concluded that the interaction between two “macrocyclic” rings in the case of the R' family does not play a significant role due to the presence of an extra phenyl group in the middle of them. The presence of the extra phenyl group increases a large separation between two “macrocycles” in the R' compound. We presented the thermochemical parameters like change in enthalpy (ΔH_{gas}) and free energy in the gas and solvent phases (ΔG_{gas} and ΔG_{solv}) in Table 6.

Thus, we examined the origin of positive cooperativity in the template-directed rotaxane compounds. The possible source of the positive cooperativity is the separation between the “macrocyclic” rings threaded over the “axle” molecule. At the optimal distance, it shows a positive cooperative effect, which can be better visualized from Figure 1. The distance between two macrocyclic rings of 2R-D-2PF₆ (R family) is 4.0 Å, whereas the distance between two –NH₂⁺– groups on the “axle” molecule is of 4.8 Å. This distinction makes clear that the “macrocyclic” rings are slightly twisted toward each other, and they are trying to interact with each other remaining at a

Table 6. ΔG_{gas} and ΔG_{solv} with Respect to Isolated Rotaxane Rings and Dumbbell^a

compound	ΔH_{gas}	ΔG_{gas}	ΔG_{solv}
1R-D-2PF ₆	−41.2	−26.1	−33.1
2R-D-2PF ₆	−85.7	−60.6	−51.4
1R-D-2I	−37.0	−22.0	−1.5
2R-D-2I	−79.0	−53.8	−54.9
1R-D-2F	−37.8	−22.8	−20.4
2R-D-2F	−39.3	−14.1	−21.4
1R-D-2	−114.1	−99.1	−46.3
2R-D-2	−88.4	−63.3	−44.1
1R-Dp-2PF ₆	−75.7	−60.6	−48.2
2R-Dp-2PF ₆	−45.7	−20.5	−25.1
1R-Dp-2I	−74.3	−59.3	−45.1
2R-Dp-2I	−32.9	−7.7	−6.5
1R-Dp-2F	−29.7	−14.6	−16.9
2R-Dp-2F	−32.5	−7.3	−2.5
1R-Dp-2	−89.1	−74.0	−40.7
2R-Dp-2	−85.0	−59.9	−37.6

^aAll the units are in kcal/mol.

minimum distance of 4.0 Å, which is very close to the ideal distance (3.6 Å) for experiencing positive cooperativity (see Figure S2a). On the other hand, the distance between two $-\text{NH}_2^+$ sites of the 2R-Dp-2PF₆ (R' family) is 7.1 Å, which is higher by $(7.1-3.6) = 3.5$ Å than the ideal value due to the presence of the extra phenyl ring in between them. This higher-order separation between two $-\text{NH}_2^+$ sites holds two “macrocyclic” rings and keeps away from each other, which is reflected in the separation distances. The distance between two macrocyclic rings is 5.0 Å in the case of the R' family. The separation is longer by 1 Å than that of the R compound. This fact ascertains the reduced degree of interaction between the “macrocyclic” rings in the rotaxane of the R' family than that present in the R family. We can see that the “macrocyclic” rings are relatively less twisted in the R' compound than in the R compound (see Figure S2d).

3.3. Role of the Counter Anion. After finding the source of the positive cooperative effect, we tried to analyze the role of PF₆[−] as a counter anion in the studied rotaxane systems. In this connection, we optimized the geometries of D, 1R-D, and 2R-D (having a charge of +2) with different counter anions like PF₆[−], F[−], and I[−] (see Figures S2 and S3). The same procedure is also done with Dp, 1R-Dp, and 2R-Dp (see Figures S2 and S4).

In general, it is observed that when the position of the counter anions is changed (by decreasing the distance between the counter anion and the $-\text{NH}_2^+$ moiety), the distance between two “macrocyclic” rings is affected. When we compared the optimized geometries for the R' family, we found that the skeletons of 2R-D are very close with both PF₆[−] and I[−] while it shows a significant difference with the F[−] counter anion. The correlation of the electron density and thermodynamic properties is reflected in a similar manner for the optimized structures of the R' family. We calculated the structures without counter anions, i.e., bare rotaxane with a +2 charge, to explore the effect of a homogeneous field versus a counter anion effect for the neutralization of systems. We calculated the distance between “macrocyclic” molecules threaded over the “axle” molecule in the presence of a counter anion. The results are given in Figure 1. We found that when only the counter anion PF₆[−] or I[−] is introduced to the compounds of the R family, and the positive cooperativity is found. It is a very interesting fact that when the

second “macrocyclic” ring is incorporated to the 1R-D system, it results in more change in free energy (more negative value). However, with the introduction of counter anions F[−], the positive cooperativity vanishes. This circumstance occurring in the gas and solvent phases is shown in Figure S5. Therefore, the effect of the counter anion is also very important for the R family especially in the presence of counter anion cooperativity coming into the picture. On the other hand, in the case of 2R-Dp compounds, there is no positive cooperativity in the presence of the counter anion PF₆[−], while it shows positive cooperativity without counter anions and with other counter anions like F[−] and I[−] (see in Figure 1 and at the bottom of Figure S5).

Furthermore, we calculated the Mulliken charges and molecular electrostatic potential (MEP) to investigate the role of the counter anion (see Table S1). Then, we employed the calculated charges to compute the dipole moments of the systems presented in Figure S6. The obtained results from Mulliken charges and MEP charges are very close, although we have discussed MEP results here. It is found that as the size of the counter anion increases, the dipole moment (μ) of the compounds under investigation increases. Therefore, we can conclude that the dipole moments of the systems are correlated with the size of the counter anions (as depicted in Figure S6). The compound having counter anion PF₆[−] shows the highest dipole moment ($\mu = 28$ Debye), where the MEP charges are localized, while the compound with counter anion F[−] has a lower dipole moment value ($\mu = 14.8$ Debye) because of more spreading of MEP charges over the compound. It seems that small counter anion F[−] interacts strongly with the $-\text{NH}_2^+$ moiety of the “axle” molecule resulting in high charge separation. Due to such interaction, the electrostatic charges on the first and second $-\text{NH}_2^+$ groups range from +0.49 to +0.36 (with counter anion F[−]) and +1.00 to +0.67 (with counter anion PF₆[−]), respectively.

Thus, the charge density on the $-\text{NH}_2^+$ recognition sites is controlled by the counter anions. The counter anions with a small size reduce the interaction strength between the “cyclic” molecules threaded over the “axle” molecule and the $-\text{NH}_2^+$ moiety present at the “axle” recognition site by virtue of reducing the charge density on N. Their consequences are the disappearance of positive cooperativity even if there is still an interaction between cyclic molecules. It is a very important aspect that the $-\text{NH}_2^+$ moiety serves as a site where the imine bond of rotaxane takes place. A similar effect arises for the compounds of the R' family. The computed dipole moment of the rotaxane compounds with the counter anion PF₆[−] is higher ($\mu = 24.9$ Debye) than that with F[−] ($\mu = 5.8$ Debye) (see Figure S6b). This is a first-time finding; our investigation suggests that the counter anion that is bulkier (softer) in size interacts less likely with the recognition site $-\text{NH}_2^+$, present in the “axle” molecule, and the interaction becomes more likely between $-\text{NH}_2^+$ and the “macrocyclic” ring.

3.4. ADMP Study. Ab initio MD simulation was performed using the ADMP^{20,21,56} simulation at different higher temperatures than room temperature (500, 700, 900, 2000, and 2500 K) on the 2R-D-2PF₆ compound. The trajectories of nuclear kinetic energy and total energy with respect to time dynamics suggest that our selected rotaxane compounds (“macrocyclic” and “axle” molecules including counter anion PF₆[−]) do not undergo dissociation at 300 and 500 K temperatures, but above the 700 K temperature, the set of “macrocyclic” molecules threaded over the “axle” molecule gets disrupted, although PF₆[−] does not go far beyond the electrostatic interaction zone. The

trajectories of 1.2 ps simulation run at all the aforementioned temperatures are presented in Figure 2 (at 300, 500, 700, and

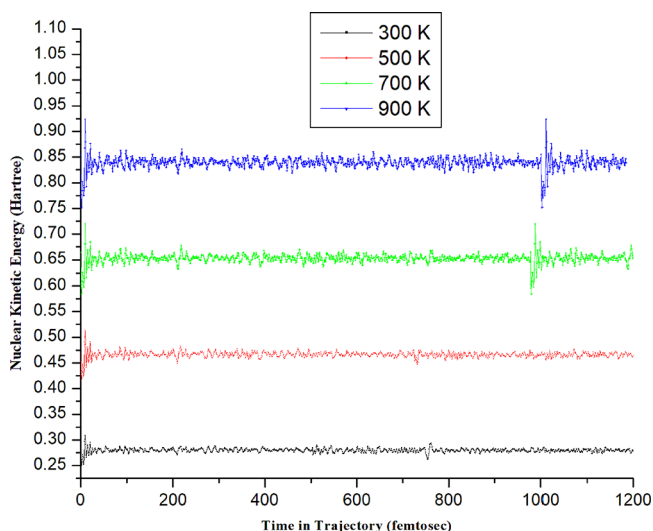


Figure 2. Trajectories at temperature 300 K obtained by performing 1.2 ps ADMP simulations for the 2R-D-2PF₆ compound.

900 K), which clearly shows that the rigid structure of rotaxane is very much sustainable even at a very high temperature, e.g., 700 K. The simulation videos are uploaded as supporting materials (see Videos S1–S8).

It is found that the PF₆[−] counter anion electrooptically interacts with the −NH₂⁺ groups of the “axle” molecule and remains in close vicinity of rotaxane. Throughout the course of the dynamical evolution (up to 1.2 ps) at 300 and 500 K temperatures, the whole compound remains at its equilibrium position without breaking the structures completely. However, at temperatures higher than 700 K, the “macrocyclic” molecules threaded over the “axle” molecule become deformed (“buckling”) from their original structure although PF₆[−] moves very slightly away from its equilibrium position. A characteristic vibrational motion is found in the P–F bonds of the counter ion PF₆[−], and a noticeable movement (which started to go away significantly from the main rotaxane moiety) is found during the course of the dynamic process at a very high temperature, e.g., 2665 K (see Table S3; the interaction free energy between PF₆[−] and 2R-D becomes zero at 2665 K). Therefore, the point is noteworthy in that during the course of the dynamical evolution, our selected rotaxane compound (2R-D-2PF₆) exhibited good dynamical or kinetic stability up to 500 K. It is evident that the counter anion’s propensity is to escape by overcoming the rotaxane congener’s binding energy, which would allow PF₆[−] to attain a higher entropic state. We studied the required exact temperature to release PF₆[−], given in Table S2.

3.5. Release of PF₆[−]. The counter anions PF₆[−] are strongly bound with the rotaxane parent moiety (2R-D), which is reflected by the binding energy per PF₆[−] −81.0 kcal/mol at 300 K. The strong electrostatic interaction is responsible for such binding counter anion. We studied the temperature effect to release PF₆[−] from the binding site of 2R-D. The temperature-induced PF₆[−] release process is shown in Table S2.

The chemical bonding and noncovalent inter- and intramolecular interactions are responsible for stabilizing the 2R-D-2PF₆ compound, which are investigated with the help of RDG and NCI indices within the optimized structure (static

structure) of rotaxane along with the aRDG and TFI plots from the ADMP simulation of 1.2 ps (averaged over 1200 structures generated from ab initio molecular dynamics simulation). For ADMP simulation at 300 K, the trajectory is saved for the 1.2 ps time window, and finally, 1200 frames were obtained. The output coordinates are exported and boot up in the Multiwfn 3.7 interface and analyzed for weak interactions. Multiwfn was used to calculate electron density, its gradient, and the Hessian of each frame, and then the average of all the quantities were evaluated. Finally, the average RDG and average sign(λ_2) ρ were evaluated. The whole process took 5.8 min on an Intel 18-core and 32 GB memory-based computer.

3.6. Analysis of Weak Interactions. To distinguish the types of weak interactions present in rotaxane compounds like van der Waals, π – π stacking, H-bonding, and steric interactions, we performed NCI analysis on the optimized geometry of rotaxane along with aNCI throughout the molecular dynamics trajectory (over 1200 trajectory points) at 300 K. The only distinction between the original NCI method and aNCI is that the former method calculates the electron density ρ and its gradient norm $|\nabla\rho|$ on one particular geometry, which is the optimized structure in our studied case, whereas aNCI evaluates the average of electron density and its first derivative (namely, $\bar{\rho}$ and $\bar{\nabla}\rho$) considering multiple structures from the dynamics process. The electron density and its first derivative ($s = 1/(2(3\pi^2)^{1/3})|\nabla\rho/\rho^{4/3}|$) collectively distinguish the NCIs and isolate the exponential decay of the electron density. The NCI method being an indicator of the interaction strength describes the regions associated with low electronic densities and the regions of small RDG. The expression of the aRDG is given as

$$\text{aRDG}(r) = 1/(2(3\pi^2)^{1/3})|\bar{\nabla}\rho(r)|/\bar{\rho}(r)^{4/3} \quad (13)$$

Similarly, the second largest eigenvalue of the averaged electron density (λ_2 term) was measured.

The Hessian matrix was assessed throughout the dynamical process to obtain the averaged weak interaction. We also performed an analysis of a new indicator called TFI similar to the aNCI method to reveal the significant stability of our selected rotaxane compound by inter- and intramolecular interactions between “macrocyclic” molecules threaded over the “axle” molecule along the dynamical process.

$$\text{TFI}(r) = \text{std}[\rho(r)]/\bar{\rho}(r) \quad (14)$$

The numerator of the above equation is the standard deviation of electron density in the dynamical trajectory and described as

$$\text{std}[\rho(r)] = \sqrt{\frac{\sum i[\rho_i(r) - \bar{\rho}(r)]^2}{n}} \quad (15)$$

n represents the number of frames in the dynamic trajectory, and ρ_i is the calculated density of the i th frame. All the weak interactions are represented with 2D GNU plots and 3D-colored isosurface plots to visually identify the regions.

Now, the question is, is it possible to describe both covalent and NCIs in the rotaxane compound by a single real space function? De Silva and Corminboeuf²⁸ proposed a density-dependent bonding descriptor named density overlap regions indicator (DORI), which can identify both covalent bonding interactions along with the noncovalent ones and identify the corresponding regions depending on the proper choice of an isovalue. The sign(λ_2) ρ mapped DORI is expressed as

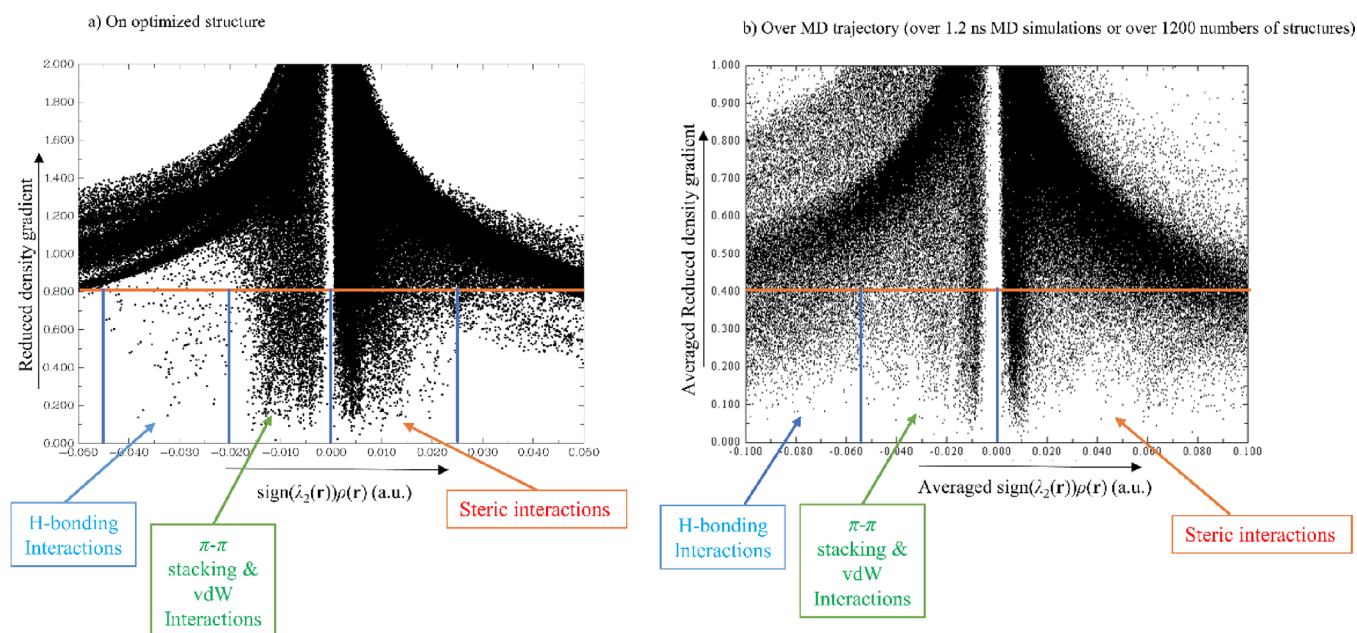


Figure 3. Plots of the reduced density gradient versus electron density ρ multiplied by the sign of the second largest eigenvalue (λ_2) of the Hessian matrix at position r on the (a) optimized structure of rotaxane and (b) average reduced density gradient versus electron density average sign(λ_2) ρ .

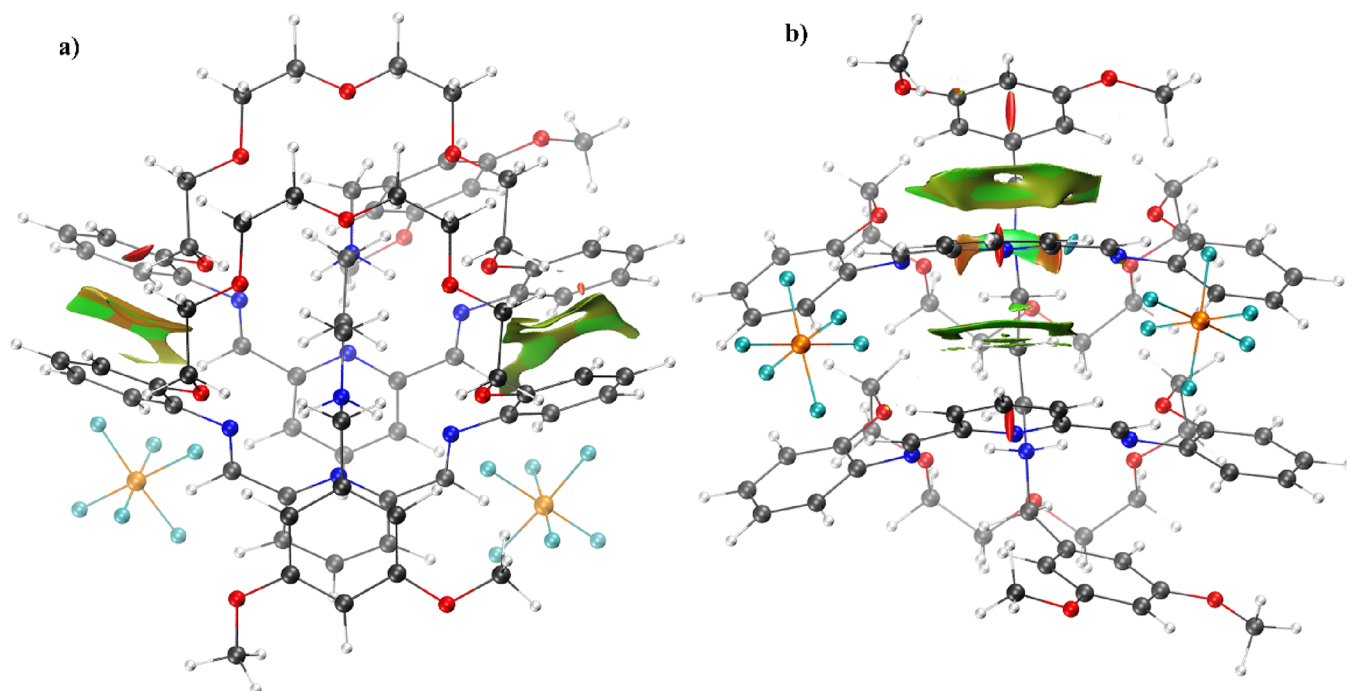


Figure 4. Three-dimensional view of $\pi \cdots \pi$ stacking interactions indicated by the gradient isosurfaces with $s = 0.5$ a.u. (green isosurface represents $\pi \cdots \pi$ stacking interactions; hydrogen, carbon, nitrogen, oxygen, fluorine, and phosphorus atoms are represented by white, black, blue, red, cyan, and orange colors).

$$\text{DORI}(r) = \frac{\theta(r)}{1 + \theta(r)} \quad (16)$$

$$\theta(r) = \frac{(\nabla k^2(r))^2}{(k^2(r))^3} = \frac{\left(\nabla \left(\frac{\nabla \rho(r)}{\rho(r)} \right)^2 \right)^2}{\left(\frac{\nabla \rho(r)}{\rho(r)} \right)^6} \quad (17)$$

We used the IRI,²⁹ which is simpler and computationally cheaper and whose graphical effect is significantly better than the DORI (only the electron density and its gradient are required to get the IRI whereas the Hessian of the electron density is required to plot the DORI).

The expression of the IRI is as follows:

$$\text{IRI}(r) = |\nabla \rho(r)| / [\rho(r)] \quad (18)$$

We performed an investigation employing all the above-mentioned methods to get a transparent representation of

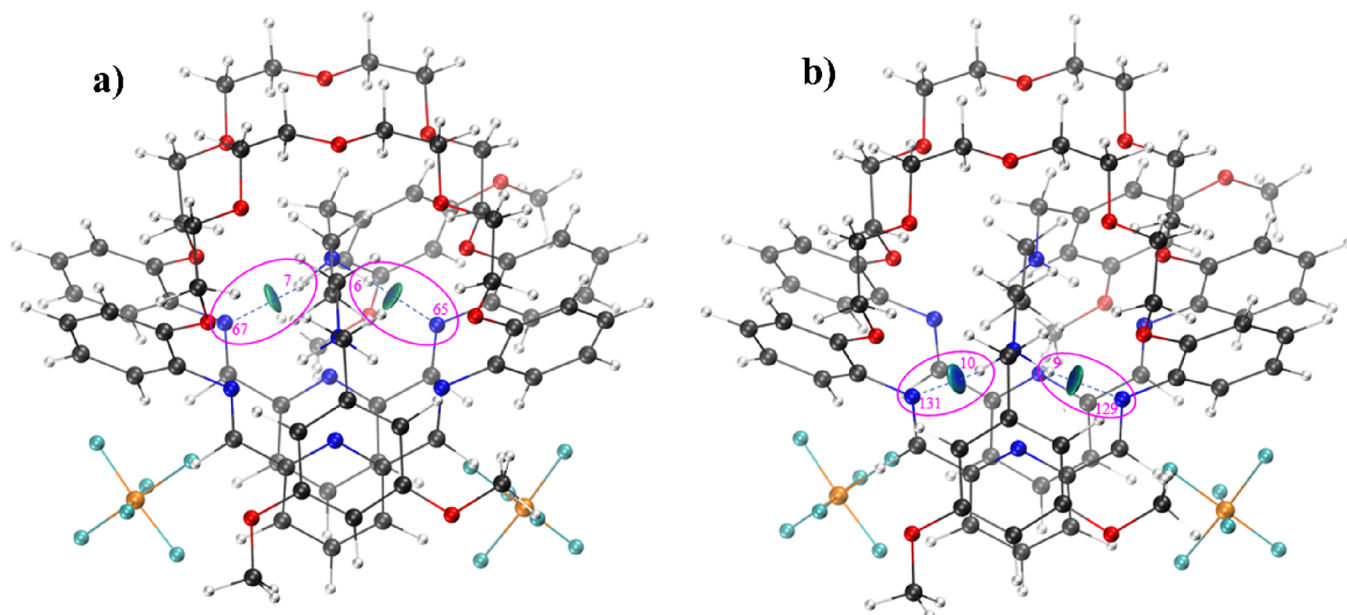


Figure 5. Three-dimensional view of hydrogen bond interactions ((a) N5-H7...N67 and N5-H6...N65, (b) N8-H10...N131 and N8-H9...N129) indicated by the gradient isosurfaces with $s = 0.5$ a.u.

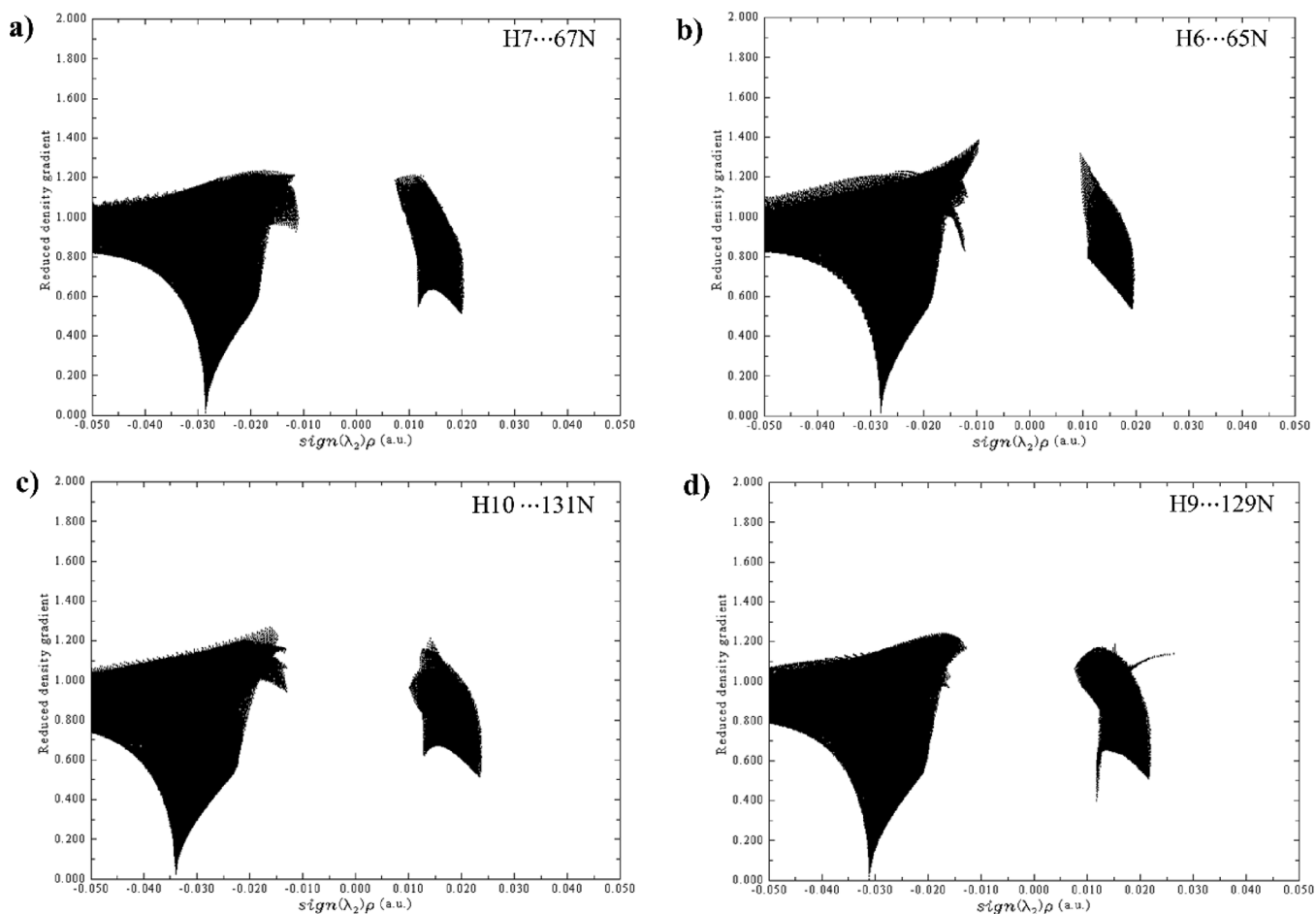


Figure 6. Two-dimensional GNU plot of four distinct hydrogen bond interactions ((a) N5-H7...N67, (b) N5-H6...N65, (c) N8-H10...N131, and (d) N8-H9...N129) indicated by reduced density gradient s versus electron density ρ multiplied by the sign of the second Hessian eigenvalue (λ_2).

noncovalent inter- and intramolecular interactions like van der Waals, $\pi \cdots \pi$ stacking, hydrogen bonding, and steric interactions besides covalent bonding into the rotaxane compound.

3.6.1. RDG. The plot of RDG versus ρ for the 2R-D-2PF₆ compound is shown as a characteristic spike(s) in the low-density region, which indicates the presence of weak NCIs such

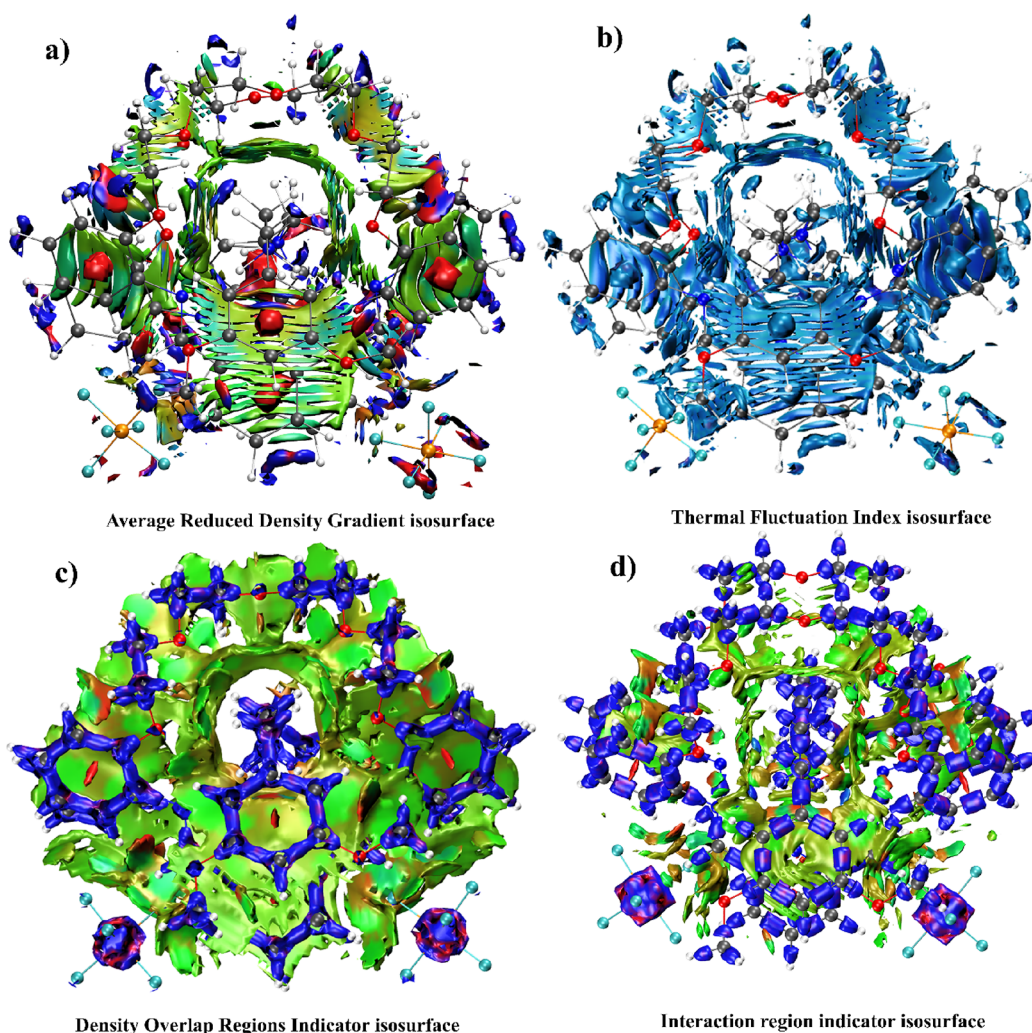


Figure 7. 3D isosurface plots of (a) aRDG, (b) TFI, (c) DORI, and (d) IRI (green-colored isosurface in (a) represents that the van der Waals interaction is major, blue-colored isosurface represents notable attraction and hydrogen bonding interactions, and red-colored isosurface represents steric interactions; blue-colored isosurface in (b) represents that the thermal fluctuation index is smaller and the corresponding regions are more stable; the color code in (c) and (d) blue–green–red represents chemical/hydrogen bond–vdW interaction–repulsive interactions).

as van der Waals, $\pi\cdots\pi$ stacking, hydrogen bonding, and steric repulsion.

Equation 13 collapses to zero at small density regions, and the three different spikes are identified on the left-side plot (RDG within the optimized compound) of Figure 3, indicating hydrogen bonding (with effective density of (-0.045) – (-0.020)), weak van der Waals attractions (with effective density of (-0.020) – 0.000 including $\pi\cdots\pi$ stacking interactions), and steric crowding around 0.000 – 0.025 regions. On the other hand, three separate spikes are observed in the aRDG plot flanked by averaged zero effective density. The spikes at the negative density regions indicate the presence of a non-separable H-bond and vdW interactions (although we considered $\rho < -0.060$ for hydrogen bonding interaction and $\rho \approx (-0.060)$ – 0.000 for vdW interactions and $\pi\cdots\pi$ stacking interactions), and the $\rho > 0.000$ region indicates steric repulsion. This investigation can be further explicitly explored by detailed analyses of the 3D RDG distribution, DORI, IRI, and Hirshfeld surface.

We have presented a visually clear 3D isosurface plot of $\pi\cdots\pi$ stacking interactions (see Figure 4) governed by two pairs of benzene rings of two “macrocyclic” molecules, between two pyridine rings of two “macrocyclic” molecules and two di-

methoxy benzene rings at stopper ends in the 2R-D-2PF₆ compound. The green isosurface (with 0.3 isovalue) in Figure 4 suggests the $\pi\cdots\pi$ attractive type of interaction holding the aromatic moieties in the rotaxane compound tightly and hindering to destroy it until a very high temperature ca. 700 K is not applied.

With careful investigation within the optimized structure, we can identify four hydrogen bonding interactions (N5–H7 \cdots N67, N5–H6 \cdots N65, N8–H10 \cdots N131, and N8–H9 \cdots N129), which are pictorially depicted in Figure 5 (3D blue-green isosurfaces) and Figure 6 (2D GNU plot). We can find the spikes in between -0.02 and -0.04 in the 2D GNU plot on the left side of Figure 3, which are distinctly shown in Figure 6, suggesting the presence of a hydrogen bond.

3.6.2. aRDG, TFI, DORI, and IRI. As shown in Figure 7, the microscopic details of the NCI regions are presented using the following analyses depending on electron density and its first and second derivatives.

It is noted that the RDG and electron localization function (ELF) can be employed together in order to study NCIs along with covalent ones at the same time. The RDG is well known to reveal identification of NCIs whereas covalent interactions can

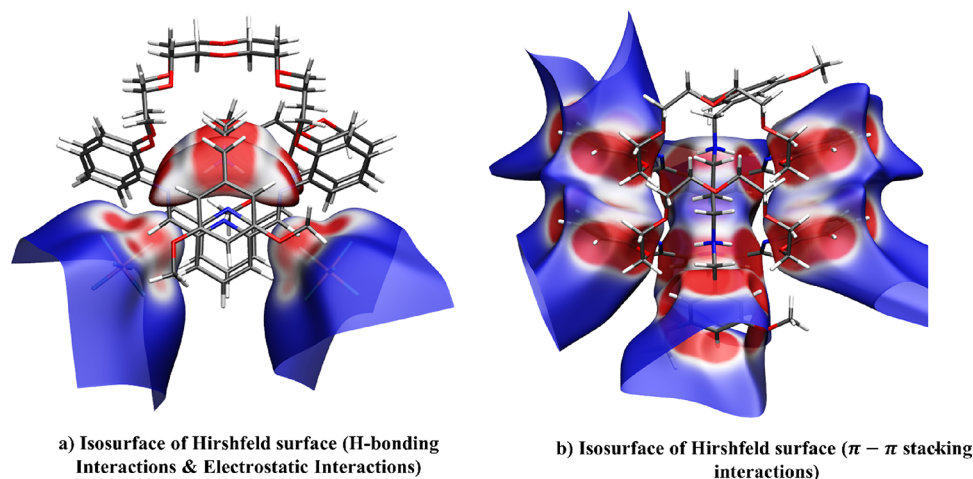


Figure 8. Plot of color-mapped isosurfaces of the Hirshfeld surface (the contacts that are shorter, equal, and longer than the van der Waals radii are referred by bright-red, white, and blue color codes)

be investigated through ELF analysis.^{57–60} However, in an analysis, consideration of two simultaneous functions is evidently very problematic. The DORI aims to reveal non-covalent and covalent interactions on an equal footing, although it has two main shortcomings: (i) the calculation of the DORI demands a second-order derivative of electron density, which leads toward more difficult situations for its implementation and evaluation, and (ii) the numerical noise in some regions of the DORI isosurface makes it an often unsatisfactory graphical effect. To avoid such shortcomings, a new real space function named IRI similar to the DORI is proposed by Lu and Chen,²⁹ by making slight modifications to the RDG. The IRI is clearly able to elucidate both chemical bonds and noncovalent weak interaction noise freely and without calculating a second derivative of electron density, which is much simpler and more cost effective (since the IRI only deals with electron density and its gradient, its implementation is advantageous for us). IRI analysis is performed by Multiwfn coding.⁴⁷ The graphical isosurface of both DORI and IRI of the rotaxane compound is presented in Figure 7. The IRI isosurface is very smooth and clear in presenting chemical bonds and notable weak interactions. The grid data calculation is carried out at the Multiwfn interface followed by VMD 1.9.3 software,⁴⁸ which is used for rendering isosurface maps.

3.6.3. Hirshfeld Surface Analysis. The Hirshfeld surface analysis was introduced first by Spackman and Byrom in 1997.⁶¹ In 2009, Spackman and Jayatilaka made a joint review,⁶² and in the last few years, the approach has become popular in studying weak interactions and crystal packing. In our present study, the Hirshfeld surface is analyzed to investigate intra- and inter-fragment surfaces of rotaxane compounds. The isosurface plot of the Hirshfeld surface visually elucidates the inter-fragment interactions (H-bonding interactions between two pairs of $-N=$ groups of two “macrocyclic” molecules and the pair of hydrogens of two $-NH_2^+$ fragments of the “axle” molecule, $\pi \cdots \pi$ stacking interactions between pyridine moieties of two “macrocyclic” molecules within them and with the end-capped di-methoxy benzene groups at the “stoppers” end) and intramolecular interactions ($\pi \cdots \pi$ stacking interactions between two pairs of benzene rings of two “macrocyclic” molecules threaded over the “axle” molecule) in rotaxane. The patterns of inter- and intramolecular contacts interlock rotaxane molecular architecture and make it rigid in the supramolecular

organization, which is the key attribute of molecular packing of the extended system. As shown in Figure 8, the Hirshfeld isosurfaces (with isovalue 0.5 a.u. and mapped with d_{norm}) curved plots with color codes bright red, white, and blue indicate the contacts that are shorter, equal, and longer than the van der Waals radii.

The bright-red spherical or oval-shaped spots are noticeable, which indicates strong bonding perceptions, electron density around π -rings, hydrogen bonding interactions, $\pi \cdots \pi$ stacking junction areas, and electrostatic interactions ($-NH_2^+$ groups of “axle” molecules and PF_6^- counter anions). The red and blue regions shown in Figure 8 correspond to negative and positive electrostatic potentials on the Hirshfeld surfaces. The Hirshfeld surface is mapped by electron density with promolecular approximation, varying from 0.0 to 0.015 a.u., and accordingly, the plotting color transition script is set to blue–white–red. This colored mapped is a direct evidence of inter- and intramolecular interaction regions, one that can easily be recognized.

3.7. Linear and Nonlinear Optical Properties. In the present study, we have also discussed both linear and nonlinear optical (NLO) behaviors of the 2R-D-2PF₆ compound, which can be used in various types of practical applications. The linear optical properties of the 2R-D-2PF₆ compound are investigated by UV–vis spectroscopy and polarizability analysis, whereas the nonlinear optical properties are inspected on the basis of its high dipole moment, including first- and second-order static and dynamic hyperpolarizabilities. The notable NLO activity of the rotaxane compound signifies its future utility as a potential candidate for nonlinear optical purposes like optical sensing, optical integrated optics, hi-tech optics, signal processing, optical computing, optical limiting, and quantum computing. The compound absorbs in the UV and visible region (found with the help of TDDFT-based calculations), which governs its efficient NLO responses.

3.8. Optical Property (UV–Visible Absorption Spectra). We have investigated ultraviolet–visible (UV–vis) absorption spectroscopy with the help of TDDFT analysis to understand the optical energy gaps of the 2R-D-2PF₆ compound and its associated electronic excited states. This investigation clearly suggests the optical responsive properties and the applicability of the studied compound. In general, the HOMO–LUMO (HOMO = highest occupied molecular

Table 7. Calculated Electronic Transitions for Associated Peaks in the UV–vis Absorption Spectra of Rotaxane Compounds Computed at the M06-L/6-31G(d) Level

systems	vertical excited-state transition levels	wavelength corresponding to peak, λ (nm)	oscillator strength (f)	excitation energy, ΔE (eV)	dominant transitions
rotaxane	S0 \rightarrow S1	487.20	0.015	2.54	HOMO \rightarrow LUMO (94.1%), HOMO \rightarrow LUMO+1 (4.8%)
rotaxane	S0 \rightarrow S2	478.34	0.004	2.59	HOMO-2 \rightarrow LUMO (6.5%), HOMO-1 \rightarrow LUMO (92.5%)
rotaxane	S0 \rightarrow S3	463.29	0.021	2.68	HOMO-3 \rightarrow LUMO (11.5%), HOMO-3 \rightarrow LUMO+1 (2.6%), HOMO-2 \rightarrow LUMO (76.6%), HOMO \rightarrow LUMO (3.3%), HOMO \rightarrow LUMO+1 (2.1%)
rotaxane	S0 \rightarrow S4	457.73	0.016	2.71	HOMO-4 \rightarrow LUMO (3.0%), HOMO-3 \rightarrow LUMO (61.8%), HOMO-2 \rightarrow LUMO (4.9%), HOMO-2 \rightarrow LUMO+1 (4.2%), HOMO-1 \rightarrow LUMO+1 (17.8%), HOMO \rightarrow LUMO+1 (5.0%)
rotaxane	S0 \rightarrow S5	452.82	0.014	2.73	HOMO-5 \rightarrow LUMO (6.6%), HOMO-4 \rightarrow LUMO (12.3%), HOMO-3 \rightarrow LUMO (11.7%),HOMO-1 \rightarrow LUMO+1 (4.4%), HOMO \rightarrow LUMO+1 (56.2%)
rotaxane	S0 \rightarrow S6	451.91	0.023	2.74	HOMO-4 \rightarrow LUMO (8.8%), HOMO-3 \rightarrow LUMO (2.9%), HOMO-2 \rightarrow LUMO (3.3%), HOMO-2 \rightarrow LUMO+1 (8.2%), HOMO-1 \rightarrow LUMO+1 (69.4%), HOMO \rightarrow LUMO+1 (3.9%)
rotaxane	S0 \rightarrow S7	447.49	0.019	2.77	HOMO-5 \rightarrow LUMO (5.0%), HOMO-4 \rightarrow LUMO (59.7%), HOMO-2 \rightarrow LUMO+1 (2.2%), HOMO \rightarrow LUMO+1 (17.3%), HOMO \rightarrow LUMO+2 (7.8%)
rotaxane	S0 \rightarrow S8	441.55	0.003	2.81	HOMO-5 \rightarrow LUMO (4.4%), HOMO-3 \rightarrow LUMO+1 (2.0%), HOMO-2 \rightarrow LUMO+1 (29.6%), HOMO \rightarrow LUMO+2 (55.1%)
rotaxane	S0 \rightarrow S9	438.65	0.005	2.82	HOMO-5 \rightarrow LUMO (65.0%), HOMO-5 \rightarrow LUMO+1 (2.6%), HOMO-4 \rightarrow LUMO (6.5%), HOMO-4 \rightarrow LUMO+1 (4.7%), HOMO-3 \rightarrow LUMO+1 (7.8%), HOMO-1 \rightarrow LUMO+2 (9.4%)
rotaxane	S0 \rightarrow S10	438.23	0.050	2.83	HOMO \rightarrow LUMO+2 (10.0%) HOMO-5 \rightarrow LUMO (5.5%), HOMO-5 \rightarrow LUMO+1 (3.3%), HOMO-4 \rightarrow LUMO+1 (2.2%), HOMO-3 \rightarrow LUMO (3.0%), HOMO-3 \rightarrow LUMO+1 (4.9%), HOMO-2 \rightarrow LUMO+1 (48.4%), HOMO-1 \rightarrow LUMO+1 (2.7%), HOMO \rightarrow LUMO+1 (3.3%),HOMO \rightarrow LUMO+2 (16.0%), HOMO \rightarrow LUMO+3 (4.2%)

orbital and LUMO = lowest unoccupied molecular orbital) energy gap provides us with the chemical reactivity and kinetic

stability of the system. A large HOMO–LUMO energy gap corresponds to low chemical reactivity and high kinetic stability

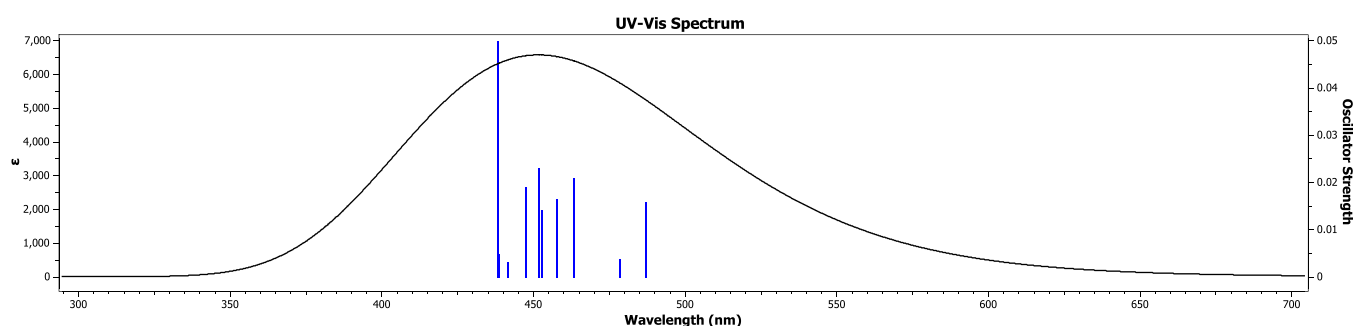


Figure 9. UV-vis absorption spectra of rotaxane in the gas phase.

Table 8. Dipole Moment (μ_e), Static and Frequency-Dependent Isotropic Polarizability (α), and Anisotropic Polarizability ($\Delta\alpha$) of Rotaxane Compounds at the M06-L/6-31G(d) Level

frequency	system	μ_e (Debye)	0.0 nm		1064.0 nm	
			$\alpha \times 10^{-24}$ (e.s.u.)	$\Delta\alpha \times 10^{-24}$ (e.s.u.)	$\alpha \times 10^{-24}$ (e.s.u.)	$\Delta\alpha \times 10^{-24}$ (e.s.u.)
	urea	3.50	3.81	2.64	3.80	2.64
	rotaxane	27.77	143.34	58.67	146.21	62.16

Table 9. First-Order and Second-Order Static and Frequency-Dependent Polarizabilities and Hyperpolarizabilities of Rotaxane Compounds at the M06-L/6-31G(d) Level

frequency	system	0.0 nm		1064.0 nm			
		$\beta(0;0,0) \times 10^{-30}$ (e.s.u.)	$\gamma(0;0,0,0) \times 10^{-36}$ (e.s.u.)	$\beta(-\omega;\omega,0) \times 10^{-30}$ (e.s.u.)	$\beta(-2\omega;\omega,\omega) \times 10^{-30}$ (e.s.u.)	$\gamma(-\omega;\omega,0,0) \times 10^{-36}$ (e.s.u.)	$\gamma(-2\omega;\omega,\omega,0) \times 10^{-36}$ (e.s.u.)
	urea	0.43	0.84	0.44	0.45	0.87	0.92
	rotaxane	10.50	186.13	18.25	58.86	255.30	963.32

because it is energetically quite unfavorable to add extra electrons in the system or especially to its high-lying LUMO.⁶³ However, such findings may not always be true if the reactivity of the systems is not solely determined by the frontier molecular orbitals (FMO).⁶⁴ However, except such a slight discrepancy, it is expected that a molecule with a small HOMO–LUMO gap is more polarizable (large α value), has a low kinetic stability and high chemical reactivity, and is denominated as a soft molecule. The energy gap between HOMO and LUMO of the 2R-D-2PF₆ compound is 2.53 eV at the M06-L/6-31G(d) level, which falls into the class of “soft molecule”. This implication leads us in deciding the outcome in linear optical response, i.e., α and the fate of the nonlinear optical response properties (hyperpolarizability), discussed in the later section. We computed vertical excitation energies (ΔE) and their associated levels, wavelengths (λ), oscillator strengths (f), and dominant contribution for the transitions (see Table 7). The UV-vis spectra of the rotaxane compound in gas phase are presented in Figure 9.

β is proportional to f and inversely proportional to ΔE associated with the corresponding electronic transition considering the standard two-level model.^{30,65} We obtained TDDFT results (Table 7) to rationalize the observed NLO behavior. From Table 7 (10 excited states are considered), we find that the 2R-D-2PF₆ compound shows the most intense electronic transition with the highest oscillator strength (f_{\max}) of 0.050 by absorbing visible radiation of 438.23 nm wavelength (λ_{\max}). The ΔE -associated transition from the S_0 to S_{10} state is 2.83 eV, and the electronic transitions were majorly associated with the molecular orbitals HOMO-5 \rightarrow LUMO (5.5%), HOMO-5 \rightarrow LUMO+1 (3.3%), HOMO-4 \rightarrow LUMO+1 (2.2%), HOMO-3 \rightarrow LUMO (3.0%), HOMO-3 \rightarrow LUMO+1 (4.9%), HOMO-2 \rightarrow LUMO+1 (48.4%), HOMO-1 \rightarrow LUMO+1 (2.7%), HOMO

\rightarrow LUMO+1 (3.3%), HOMO \rightarrow LUMO+2 (16.0%), and HOMO \rightarrow LUMO+3 (4.2%). The next significant absorption peak arises at $S_0 \rightarrow S_6$ followed by $S_0 \rightarrow S_3$, $S_0 \rightarrow S_7$, $S_0 \rightarrow S_{11}$, and so on. Relevant wavelengths for the corresponding transitions suggest that 2R-D-2PF₆ absorbs in the UV-vis domain.

3.9. Nonlinear Optical Properties. To provide linear and NLO activities of the 2R-D-2PF₆ compound, numerous investigations were carried out on the electric dipole moment, static, and dynamic (frequency-dependent) molecular polarizability, anisotropy of polarizability, and first- and second-order hyperpolarizability here.

The molecules or clusters having higher magnitudes of electric dipole moment, polarizability, and hyperpolarizability exhibit better NLO activity. The results of all these factors at the M06-L/6-31G(d) level are presented in Tables 8 and 9. The calculated dipole moment (μ_e), isotropic polarizability (actual average polarizability designated as α here), and anisotropic polarizability ($\Delta\alpha$) for 2R-D-2PF₆ are found ca. 27.77 Debye, 143.34×10^{-24} e.s.u. (at zero frequency) and 146.21×10^{-24} e.s.u. (at 1046 nm frequency), and 58.67×10^{-24} e.s.u. (at zero frequency) and 62.16×10^{-24} e.s.u. (at 1046 nm frequency), respectively. The calculated first- and second-order static hyperpolarizabilities ($\beta(0;0,0)$ and $\gamma(0;0,0,0)$) and frequency-dependent first hyperpolarizabilities such as $\beta(-\omega;\omega,0)$ for the electro-optical Pockels effect (EOPE), $\beta(-2\omega;\omega,\omega)$ for the second harmonic generation (SHG), and frequency-dependent second hyperpolarizabilities such as $\gamma(-\omega;\omega,0,0)$ for electric field-induced second harmonic (EFISH) and $\gamma(-2\omega;\omega,\omega,0)$ for electro-optical Kerr effect (EOKE) are 10.50×10^{-30} e.s.u. and 186.13×10^{-36} e.s.u., 18.25×10^{-30} e.s.u., 58.86×10^{-36} e.s.u., and 255.30×10^{-36} e.s.u. 963.32×10^{-36} e.s.u., respectively.

For comparison purposes, urea is generally used as a reference molecule for the study of nonlinear optical properties. The calculated values of the μ_e , α , and $\Delta\alpha$ of urea are 3.50 Debye, 3.81×10^{-24} e.s.u. (at zero frequency) and 3.80×10^{-24} e.s.u. (at 1046 nm frequency), and 2.64×10^{-24} e.s.u. (at both zero and 1046 nm frequencies), respectively. The calculated $\beta(0; 0, 0)$, $\beta(-\omega; \omega, 0)$, and $\beta(-2\omega; \omega, \omega)$ are 0.43×10^{-30} e.s.u., 0.44×10^{-30} e.s.u., and 0.45×10^{-30} e.s.u. while $\gamma(0; 0, 0, 0)$, $\gamma(-\omega; \omega, 0, 0)$, and $\gamma(-2\omega; \omega, \omega, 0)$ are 0.84×10^{-36} e.s.u., 0.87×10^{-36} e.s.u., and 0.92×10^{-36} e.s.u. It is noticed that the calculated dipole moment, isotropic static polarizability, and polarizability at the 1064 nm frequency of the 2R-D-2PF₆ compound are nearly 7.93, 37.62, and 38.48 times greater than those of urea, whereas anisotropic polarizabilities at zero and 1064 nm frequencies are nearly 22.22 and 23.55 times greater, respectively. The static first- and second-order hyperpolarizabilities of 2R-D-2PF₆ compared to urea are 24.42 and 221.58 times greater, whereas the first- and second-order hyperpolarizabilities at 1064 nm for EOPE, SHG, EFISH, and EOKE are 41.48, 130.8, 293.45, and 1047.09 times, respectively. Very large values of all these NLO descriptors of the 2R-D-2PF₆ compound ensure that it is highly recommended for nonlinear optical applications.

4. CONCLUSIONS

Our theoretical investigation of electronic structure, binding insights, thermochemical parameters, and nonlinear optical properties of rotaxane compound provides a clear idea in the present study. In general, all Dreiding and OPLS-based FF methods provide us with poor thermodynamic representation, although they are an acceptable representation on a structural basis. On the other hand, the QM method provides physically meaningful and more consistent results. At the optimal distance, the interactions between “macrocyclic” rings are the source of positive cooperativity in formation of the template-directed rotaxane compounds (R family). On the other hand, the longer distance between “macrocyclic” rings for the R' family makes the interactions negligible. Therefore, from the above observation it is clear that the efficiency of the template-directed synthesis of rotaxane compounds can be tuned up by monitoring the distance between recognition sites. The counterion effect is also significant for charge distribution, which controls the clipping mechanism. Binding energy and ADMP simulation suggest that our selected rotaxane compound is thermodynamically and kinetically stable at ambient temperatures. Above the 500 K temperature, the compound shows a buckling behavior. Weak NCIs like van der Waals attractive forces, $\pi \cdots \pi$ stacking, and hydrogen bonding besides the covalent bonding interactions hold the set of “macrocyclic” molecules together with the “axle” molecule and give the rotaxane compound great stability. The TDDFT study interprets that rotaxane absorbs at the UV–visible domain, which is indicative of the system to be used for solar radiation capturing purposes. Furthermore, linear and nonlinear optical property studies suggest that rotaxane is a very promising optical material, which reflects its future applicability for the same.

■ ASSOCIATED CONTENT

SI Supporting Information

The Supporting Information is available free of charge at <https://pubs.acs.org/doi/10.1021/acs.jpca.2c07774>.

Computational details; comparison of XRD experimentally determined structures versus different theoretical methods used; compounds for the R family and for the R' family; xR-D-2anion compounds; xR-Dp-2anion compounds; free energies in the gas phase for the gas phase and solvated phase for the R family; dipole moments (μ) from ESP charges; dipole moments (μ , /Debye) obtained from electrostatic potential (ESP) charges and Mulliken charges; free energy change (ΔG , kcal·mol^{−1}) at different temperatures for the dissociation process; free energies in the gas and solvated phases including quantum corrections; electronic energy (E_{scf}), zero-point energy (ZPE), solvation energy for CH₃CN; free energies in the gas and solvated phases including quantum corrections; electronic energy (E , scf), zero-point energy (ZPE), solvation energy for CH₃CN (E_{solv}); first-order and second-order static and frequency-dependent polarizabilities and hyperpolarizabilities of rotaxane compounds at CAM-B3LYP/6-31+G(d) level; coordinates of the optimized structures (PDF)

ADMP simulation (1.2 ps) videos at 300, 500, 700, and 900 K for the rotaxane compound, 2R-D-2PF₆ (ZIP)

■ AUTHOR INFORMATION

Corresponding Author

Jose L. Mendoza-Cortes – Department of Chemical Engineering and Materials Science, Michigan State University, East Lansing, Michigan 48824, United States; orcid.org/0000-0001-5184-1406; Email: jmendoza@msu.edu

Author

Gourhari Jana – Department of Chemical Engineering and Materials Science, Michigan State University, East Lansing, Michigan 48824, United States; orcid.org/0000-0001-7864-8489

Complete contact information is available at: <https://pubs.acs.org/10.1021/acs.jpca.2c07774>

Author Contributions

All authors have given approval to the final version of the manuscript.

Notes

The authors declare no competing financial interest.

■ ACKNOWLEDGMENTS

This work was supported in part through computational resources and services provided by the Institute for Cyber-Enabled Research at Michigan State University. G.J. and J.L.M.-C. thank the computational resources and services provided by the Institute for Cyber-Enabled Research at Michigan State University.

■ REFERENCES

- (1) Erbas-Cakmak, S.; Leigh, D. A.; McTernan, C. T.; Nussbaumer, A. L. Artificial molecular machines. *Chem. Rev.* **2015**, *115*, 10081–10206.
- (2) Mayumi, K.; Ito, K.; Kato, K. *Polyrotaxane and slide-ring materials*; Royal Society of Chemistry: Cambridge, UK, 2015.
- (3) Fang, L.; Olson, M. A.; Benítez, D.; Tkatchouk, E.; Goddard, W. A., III; Stoddart, J. F. Mechanically bonded macromolecules. *Chem. Soc. Rev.* **2010**, *39*, 17–29.
- (4) Collin, J. P.; Dietrich-Buchecker, C.; Gaviña, P.; Jimenez-Molero, M. C.; Sauvage, J. P. Shuttles and muscles: linear molecular machines based on transition metals. *Acc. Chem. Res.* **2001**, *34*, 477–487.

- (5) Berná, J.; Leigh, D. A.; Lubomska, M.; Mendoza, S. M.; Pérez, E. M.; Rudolf, P.; Teobaldi, G.; Zerbetto, F. Macroscopic transport by synthetic molecular machines. *Nat. Mater.* **2005**, *4*, 704–710.
- (6) Kottas, G. S.; Clarke, L. I.; Horinek, D.; Michl, J. Artificial molecular rotors. *Chem. Rev.* **2005**, *105*, 1281–1376.
- (7) Balzani, V.; Credi, A.; Venturi, M. Light powered molecular machines. *Chem. Soc. Rev.* **2009**, *38*, 1542–1550.
- (8) Spruell, J. M.; Paxton, W. F.; Olsen, J.-C.; Benítez, D.; Tkatchouk, E.; Stern, C. L.; Trabolsi, A.; Friedman, D. C.; Goddard, W. A., III; Stoddart, J. F. A push-button molecular switch. *J. Am. Chem. Soc.* **2009**, *131*, 11571–11580.
- (9) Klajn, R.; Stoddart, J. F.; Grzybowski, B. A. Nanoparticles functionalised with reversible molecular and supramolecular switches. *Chem. Soc. Rev.* **2010**, *39*, 2203–2237.
- (10) Lim, J. Y. C.; Marques, I.; Félix, V.; Beer, P. D. A chiral halogen-bonding [3] rotaxane for the recognition and sensing of biologically relevant dicarboxylate anions. *Angew. Chem. Int. Ed.* **2018**, *57*, 584–588.
- (11) Feringa, B. L. The art of building small: From molecular switches to motors (Nobel lecture). *Angew. Chem. Int. Ed.* **2017**, *56*, 11060–11078.
- (12) Sauvage, J. P. From chemical topology to molecular machines (Nobel lecture). *Angew. Chem. Int. Ed.* **2017**, *56*, 11080–11093.
- (13) Stoddart, J. F. Mechanically interlocked molecules (MIMs)-molecular shuttles, switches, and machines (Nobel Lecture). *Angew. Chem. Int. Ed.* **2017**, *56*, 11094–11125.
- (14) Aricó, F.; Badjic, J. D.; Cantrill, S. J.; Flood, A. H.; Leung, K. C.-F.; Liu, Y.; Stoddart, J. F. Templated synthesis of interlocked molecules. *Templates Chem. II* **2005**, 203–259.
- (15) Horn, M.; Ihringer, J.; Glink, P. T.; Stoddart, J. F. Kinetic versus thermodynamic control during the formation of [2] rotaxanes by a dynamic template-directed clipping process. *Chem. Eur. J.* **2003**, *9*, 4046–4054.
- (16) Brady, P. A.; Sanders, J. K. M. Selection approaches to catalytic systems. *Chem. Soc. Rev.* **1997**, *26*, 327–336.
- (17) Corbett, P. T.; Leclaire, J.; Vial, L.; West, K. R.; Wietor, J.-L.; Sanders, J. K. M.; Otto, S. Dynamic combinatorial chemistry. *Chem. Rev.* **2006**, *106*, 3652–3711.
- (18) Meyer, C. D.; Joiner, C. S.; Stoddart, J. F. Template-directed synthesis employing reversible imine bond formation. *Chem. Soc. Rev.* **2007**, *36*, 1705–1723.
- (19) Belowich, M. E.; Valente, C.; Smaldone, R. A.; Friedman, D. C.; Thiel, J.; Cronin, L.; Stoddart, J. F. Positive cooperativity in the template-directed synthesis of monodisperse macromolecules. *J. Am. Chem. Soc.* **2012**, *134*, 5243–5261.
- (20) Schlegel, H. B.; Millam, J. M.; Iyengar, S. S.; Voth, G. A.; Daniels, A. D.; Scuseria, G. E.; Frisch, M. J. Ab initio molecular dynamics: Propagating the density matrix with Gaussian orbitals. *J. Chem. Phys.* **2001**, *114*, 9758–9763.
- (21) Schlegel, H. B.; Iyengar, S. S.; Li, X.; Millam, J. M.; Voth, G. A.; Scuseria, G. E.; Frisch, M. J. Ab initio molecular dynamics: Propagating the density matrix with Gaussian orbitals. III. Comparison with Born–Oppenheimer dynamics. *J. Chem. Phys.* **2002**, *117*, 8694–8704.
- (22) Scuseria, G. E. Linear scaling density functional calculations with Gaussian orbitals. *J. Phys. Chem. A* **1999**, *103*, 4782–4790.
- (23) Marx, D.; Hutter, J. *Modern methods and algorithms of quantum chemistry*; Grotendorst, J., Ed.; NIC, 2000, 301, 449.
- (24) Barnett, R. N.; Landman, U. Born–Oppenheimer molecular-dynamics simulations of finite systems: Structure and dynamics of (H₂O)₂. *Phys. Rev. B* **1993**, *48*, 2081.
- (25) Iyengar, S. S.; Schlegel, H. B.; Millam, J. M.; A. Voth, G.; Scuseria, G. E.; Frisch, M. J. Ab initio molecular dynamics: Propagating the density matrix with Gaussian orbitals. II. Generalizations based on mass-weighting, idempotency, energy conservation and choice of initial conditions. *J. Chem. Phys.* **2001**, *115*, 10291–10302.
- (26) Johnson, E. R.; Keinan, S.; Mori-Sánchez, P.; Contreras-García, J.; Cohen, A. J.; Yang, W. Revealing noncovalent interactions. *J. Am. Chem. Soc.* **2010**, *132*, 6498–6506.
- (27) Wu, P.; Chaudret, R.; Hu, X.; Yang, W. Noncovalent interaction analysis in fluctuating environments. *J. Chem. Theory Comput.* **2013**, *9*, 2226–2234.
- (28) De Silva, P.; Corminboeuf, C. Simultaneous visualization of covalent and noncovalent interactions using regions of density overlap. *J. Chem. Theory Comput.* **2014**, *10*, 3745–3756.
- (29) Lu, T.; Chen, Q. Interaction region indicator: A simple real space function clearly revealing both chemical bonds and weak interactions. *Chem.-Methods* **2021**, *1*, 231–239.
- (30) Kanis, D. R.; Ratner, M. A.; Marks, T. J. Design and construction of molecular assemblies with large second-order optical nonlinearities. Quantum chemical aspects. *Chem. Rev.* **1994**, *94*, 195–242.
- (31) Geskin, V. M.; Lambert, C.; Brédas, J.-L. Origin of high second- and third-order nonlinear optical response in ammonio/borato diphenylpolyene zwitterions: the remarkable role of polarized aromatic groups. *J. Am. Chem. Soc.* **2003**, *125*, 15651–15658.
- (32) Sajjan, D.; Joe, H.; Jayakumar, V. S.; Zaleski, J. Structural and electronic contributions to hyperpolarizability in methyl p-hydroxy benzoate. *J. Mol. Struct.* **2006**, *785*, 43–53.
- (33) Boulon, M.-E.; Fernandez, A.; Moreno Pineda, E.; Chilton, N. F.; Timco, G.; Fielding, A. J.; Winpenny, R. E. P. Measuring Spin–Spin Interactions between Heterospins in a Hybrid [2] Rotaxane. *Angew. Chem. Int. Ed.* **2017**, *56*, 3876–3879.
- (34) Mayo, S. L.; Olafson, B. D.; Goddard, W. A. DREIDING: a generic force field for molecular simulations. *J. Phys. Chem.* **1990**, *94*, 8897–8909.
- (35) Jorgensen, W. L.; Maxwell, D. S.; Tirado-Rives, J. Development and testing of the OPLS all-atom force field on conformational energetics and properties of organic liquids. *J. Am. Chem. Soc.* **1996**, *118*, 11225–11236.
- (36) Rappe, A. K.; Goddard, W. A., III Charge equilibration for molecular dynamics simulations. *J. Phys. Chem.* **1991**, *95*, 3358–3363.
- (37) Zhao, Y.; Truhlar, D. G. A new local density functional for main-group thermochemistry, transition metal bonding, thermochemical kinetics, and noncovalent interactions. *J. Chem. Phys.* **2006**, *125*, 194101.
- (38) Zhao, Y.; Truhlar, D. G. The M06 suite of density functionals for main group thermochemistry, thermochemical kinetics, noncovalent interactions, excited states, and transition elements: two new functionals and systematic testing of four M06-class functionals and 12 other functionals. *Theor. Chem. Acc.* **2008**, *120*, 215–241.
- (39) Clark, T.; Chandrasekhar, J.; Spitznagel, G. W.; Schleyer, P. V. R. Efficient diffuse function-augmented basis sets for anion calculations. III. The 3-21+G basis set for first-row elements, Li–F. *J. Comput. Chem.* **1983**, *4*, 294–301.
- (40) Frisch, M. J.; Pople, J. A.; Binkley, J. S. Self-consistent molecular orbital methods 25. Supplementary functions for Gaussian basis sets. *J. Chem. Phys.* **1984**, *80*, 3265–3269.
- (41) Hay, P. J.; Wadt, W. R. Ab initio effective core potentials for molecular calculations. Potentials for K to Au including the outermost core orbitals. *J. Chem. Phys.* **1985**, *82*, 299–310.
- (42) Bochevarov, A. D.; Harder, E.; Hughes, T. F.; Greenwood, J. R.; Braden, D. A.; Philipp, D. M.; Rinaldo, D.; Halls, M. D.; Zhang, J.; Friesner, R. A. Jaguar: A high-performance quantum chemistry software program with strengths in life and materials sciences. *Int. J. Quantum Chem.* **2013**, *113*, 2110–2142.
- (43) Tannor, D. J.; Marten, B.; Murphy, R.; Friesner, R. A.; Sitkoff, D.; Nicholls, A.; Honig, B.; Ringnalda, M.; Goddard, W. A., III Accurate first principles calculation of molecular charge distributions and solvation energies from ab initio quantum mechanics and continuum dielectric theory. *J. Am. Chem. Soc.* **1994**, *116*, 11875–11882.
- (44) Benítez, D.; Tkatchouk, E.; Yoon, I.; Stoddart, J. F.; Goddard, W. A. Experimentally-based recommendations of density functionals for predicting properties in mechanically interlocked molecules. *J. Am. Chem. Soc.* **2008**, *130*, 14928–14929.
- (45) Frisch, M.; Trucks, G.; Schlegel, H.; Scuseria, G.; Robb, M.; Cheeseman, J.; Scalmani, G.; Barone, V.; Petersson, G.; Nakatsuji, H. *Gaussian 16 Rev. C. 01*, Gaussian, Inc.: Wallingford, CT. 2016.

- (46) Rassolov, V. A.; Pople, J. A.; Ratner, M. A.; Windus, T. L. 6-31G* basis set for atoms K through Zn. *J. Chem. Phys.* **1998**, *109*, 1223–1229.
- (47) Lu, T.; Chen, F. Multiwfn: a multifunctional wavefunction analyzer. *J. Comput. Chem.* **2012**, *33*, 580–592.
- (48) Humphrey, W.; Dalke, A.; Schulten, K. VMD: visual molecular dynamics. *J. Mol. Graphics* **1996**, *14*, 33–38.
- (49) Pal, S.; Manna, A. K.; Pati, S. K. The role of H bonding and dipole-dipole interactions on the electrical polarizations and charge mobilities in linear arrays of urea, thiourea, and their derivatives. *J. Chem. Phys.* **2008**, *129*, 204301.
- (50) Günter, P. *Nonlinear optical effects and materials*; Springer, 2012.
- (51) Dettmar, C. M. *Second harmonic generation for probing nanoscopic order within biological systems*; Doctoral dissertation, Purdue University, 2014.
- (52) Oudar, J.-L.; Chemla, D. S. Hyperpolarizabilities of the nitroanilines and their relations to the excited state dipole moment. *J. Chem. Phys.* **1977**, *66*, 2664–2668.
- (53) Oudar, J. L.; Zyss, J. Structural dependence of nonlinear-optical properties of methyl-(2, 4-dinitrophenyl)-aminopropanoate crystals. *Phys. Rev. A* **1982**, *26*, 2016.
- (54) Bishop, D. M. *Molecular vibration and nonlinear optics*. Advances in Chemical Physics (John Wiley & Sons, Inc., 2007); 1998, 1–40.
- (55) Pati, S. K.; Marks, T. J.; Ratner, M. A. Conformationally tuned large two-photon absorption cross sections in simple molecular chromophores. *J. Am. Chem. Soc.* **2001**, *123*, 7287–7291.
- (56) Zhang, Y.; Xu, Z.; Zhao, Y.; Zhang, X. Ab initio molecular dynamics simulation study of dissociation electron attachment to lactic acid and isomer. *Sci. Rep.* **2019**, *9*, 19532.
- (57) Lu, T.; Chen, F.-W. Meaning and functional form of the electron localization function. *Acta Phys.-Chim. Sin.* **2011**, *27*, 2786–2792.
- (58) Lu, T.; Chen, Q. Revealing molecular electronic structure via analysis of valence electron density. *Acta Phys.-Chim. Sin.* **2018**, *34*, 503–513.
- (59) Becke, A. D.; Edgecombe, K. E. A simple measure of electron localization in atomic and molecular systems. *J. Chem. Phys.* **1990**, *92*, 5397–5403.
- (60) Gillet, N.; Chaudret, R.; Contreras-García, J.; Yang, W.; Silvi, B.; Piquemal, J.-P. Coupling quantum interpretative techniques: another look at chemical mechanisms in organic reactions. *J. Chem. Theory Comput.* **2012**, *8*, 3993–3997.
- (61) Spackman, M. A.; Byrom, P. G. A novel definition of a molecule in a crystal. *Chem. Phys. Lett.* **1997**, *267*, 215–220.
- (62) Spackman, M. A.; Jayatilaka, D. Hirshfeld surface analysis. *CrystEngComm* **2009**, *11*, 19–32.
- (63) Orbital, F. *Organic Chemical Reactions*; Reference Edition John Wiley & Sons, Ltd Chichester, 1976, 256, 368.
- (64) Karamanis, P.; Otero, N.; Pouchan, C. Unleashing the quadratic nonlinear optical responses of graphene by confining white-graphene (h-BN) sections in its framework. *J. Am. Chem. Soc.* **2014**, *136*, 7464–7473.
- (65) Oudar, J. L.; Chemla, D. S.; Batifol, E. Optical nonlinearities of various substituted benzene molecules in the liquid state, and comparison with solid state nonlinear susceptibilities. *J. Chem. Phys.* **1977**, *66*, 1626.

Recommended by ACS

Rydberg Macrodimers: Diatomic Molecules on the Micrometer Scale

Simon Hollerith and Johannes Zeiher

MARCH 28, 2023

THE JOURNAL OF PHYSICAL CHEMISTRY A

READ 

A Model for the Rapid Assessment of Solution Structures for 24-Atom Macrocycles: The Impact of β -Branched Amino Acids on Conformation

Alexander J. Menke, Eric E. Simanek, *et al.*

FEBRUARY 13, 2023

THE JOURNAL OF ORGANIC CHEMISTRY

READ 

Mechanical Bonding as a Promoter of Crystalline Diversity in Halogenated [2]Rotaxanes

Tainára Orlando, Jose Berna, *et al.*

APRIL 20, 2023

CRYSTAL GROWTH & DESIGN

READ 

Effect of Ring Rigidity on the Statics and Dynamics of Linear Catenanes

Pietro Chiarantoni and Cristian Micheletti

MAY 18, 2022

MACROMOLECULES

READ 

Get More Suggestions >